

Article

Novel Landfill-Gas-to-Biomethane Route Using a Gas–Liquid Membrane Contactor for Decarbonation/Desulfurization and Selexol Absorption for Siloxane Removal

Guilherme Pereira da Cunha , José Luiz de Medeiros *  and Ofélia de Queiroz F. Araújo 

Escola de Química, Federal University of Rio de Janeiro, CT, E, Ilha do Fundão, Rio de Janeiro 21941-909, RJ, Brazil; guilherme@eq.ufrj.br (G.P.d.C.); ofelia@eq.ufrj.br (O.d.Q.F.A.)

* Correspondence: jlm@eq.ufrj.br

Abstract: A new landfill-gas-to-biomethane process prescribing decarbonation/desulfurization via gas–liquid membrane contactors and siloxane absorption using Selexol are presented in this study. Firstly, an extension for an HYSYS simulator was developed as a steady-state gas–liquid contactor model featuring: (a) a hollow-fiber membrane contactor for countercurrent/parallel contacts; (b) liquid/vapor mass/energy/momentum balances; (c) CO₂/H₂S/CH₄/water fugacity-driven bidirectional transmembrane transfers; (d) temperature changes from transmembrane heat/mass transfers, phase change, and compressibility effects; and (e) external heat transfer. Secondly, contactor batteries using a countercurrent contact and parallel contact were simulated for selective landfill-gas decarbonation/desulfurization with water. Several separation methods were applied in the new process: (a) a water solvent gas–liquid contactor battery for adiabatic landfill-gas decarbonation/desulfurization; (b) water regeneration via high-pressure strippers, reducing the compression power for CO₂ exportation; and (c) siloxane absorption with Selexol. The results show that the usual isothermal/isobaric contactor simplification is unrealistic at industrial scales. The process converts water-saturated landfill-gas (CH₄ = 55.7%mol, CO₂ = 40%mol, H₂S = 150 ppm-mol, and Siloxanes = 2.14 ppm-mol) to biomethane with specifications of CH₄^{MIN} = 85%mol, CO₂^{MAX} = 3%mol, H₂S^{MAX} = 10 mg/Nm³, and Siloxanes^{MAX} = 0.03 mg/Nm³. This work demonstrates that the new model can be validated with bench-scale literature data and used in industrial-scale batteries with the same hydrodynamics. Once calibrated, the model becomes economically valuable since it can: (i) predict industrial contactor battery performance under scale-up/scale-down conditions; (ii) detect process faults, membrane leakages, and wetting; and (iii) be used for process troubleshooting.

Keywords: landfill-gas; biomethane; CO₂ removal; H₂S removal; gas–liquid membrane contactor; siloxane removal



Citation: da Cunha, G.P.; de Medeiros, J.L.; Araújo, O.d.Q.F. Novel Landfill-Gas-to-Biomethane Route Using a Gas–Liquid Membrane Contactor for Decarbonation/Desulfurization and Selexol Absorption for Siloxane Removal. *Processes* **2024**, *12*, 1667. <https://doi.org/10.3390/pr12081667>

Academic Editor: Leandro V. A. Gurgel

Received: 26 June 2024

Revised: 4 August 2024

Accepted: 6 August 2024

Published: 8 August 2024



Copyright: © 2024 by the authors. Licensee MDPI, Basel, Switzerland. This article is an open access article distributed under the terms and conditions of the Creative Commons Attribution (CC BY) license (<https://creativecommons.org/licenses/by/4.0/>).

1. Introduction

Landfills spontaneously release gases that entail sanitary, safety, and environmental issues, such as odors, combustion/explosion risks, and greenhouse gas emissions [1]. These gases are generically known as landfill-gas. Landfill-gas is generated by the anaerobic degradation of organic wastes in landfills and typically contains methane (CH₄) (30–65 %mol), carbon dioxide (CO₂) (25–47 %mol), hydrogen sulfide (H₂S) (30–500 ppm-mol), saturation water, and trace silicon compounds (0.3–36 ppm-mass dry basis). Landfill-gas may also contain nitrogen/oxygen from air, ammonia, and hydrogen [2]. The greenhouse warming potential of CH₄ is ≈21 times that of its CO₂ counterpart and landfill-gas releases are responsible for ≈17% of worldwide CH₄ emissions [3]. Moreover, landfill-gas can be converted into biomethane, so that sustainable landfills can be designed to simultaneously avoid CH₄ emissions while exporting biomethane [4] for use as, for example, household fuel-gas, renewable electricity generation [5], vehicular fuel-gas [6], and as a natural gas (NG) substitute [7].

The landfill-gas-to-biomethane process can accelerate energy transition to a low-carbon economy while ensuring energy supply, since solar photovoltaic and wind power energy are naturally intermittent [8] and are in the early development stage [9]. In this case, biomethane is delivered to pipeline networks, as well as associated and non-associated NGs [10], and unconventional NGs from shale-gas [11]. Another possibility is the landfill-gas-to-wire process, which consists of direct electricity generation dismissing purification/transportation [12].

Efficient landfill-gas recovery depends on several factors, such as the coating process, gas drainage, and leachate management [13]. In a capped landfill, landfill-gas is collected and processed to create NGs or biomethane specifications, i.e., via CO₂/H₂S removal, dehydration, and siloxane removal [14]. The landfill-gas-to-biomethane process starts with decarbonation, which increases the heating value, reduces the transportation volume, and minimizes CO₂ emissions from combustion [15]. Desulfurization is the next step aiming at reducing H₂S corrosiveness, toxicity, and acid rain potential [16]. Lastly, dehydration is conducted to avoid gas hydrates and condensation in pipelines [17].

Siloxanes are organosilicon compounds inexistent in nature containing Si-O-Si bonds and methyl groups attached to silicon atoms [18]. Landfill-gas siloxanes result from the decomposition of wastes containing silicon compounds (e.g., paints, coats/waxes, and shampoos/cosmetics) [19]. Siloxanes must be removed from landfill-gas because their oxidation in combustion engines creates SiO₂ deposits on metallic surfaces causing abrasion. In gas turbines, SiO₂ deposits cause blade erosion [20]. Table 1 shows typical landfill-gas siloxanes.

Table 1. Landfill-gas silicon compounds with typical contents [18,20].

Name	ID	Formula	Molar Mass (g/mol)	Content (mg/Nm ³)
Hexamethyl-disiloxane	L2	C ₆ H ₁₈ OSi ₂	162.38	6.07
Octamethyl-trisiloxane	L3	C ₈ H ₂₄ O ₂ Si ₃	236.53	-
Decamethyl-tetrasiloxane	L4	C ₁₀ H ₃₀ O ₃ Si ₄	310.69	0.04
Dodecamethyl-pentasiloxane	L5	C ₁₂ H ₃₆ O ₄ Si ₅	384.84	-
Tetradecamethyl-hexasiloxane	L6	C ₁₄ H ₄₂ O ₅ Si ₆	458.99	0.01
Hexamethyl-cyclotrisiloxane	D3	C ₆ H ₁₈ O ₃ Si ₃	222.46	0.49
Octamethyl-cyclotetrasiloxane	D4	C ₈ H ₂₄ O ₄ Si ₄	296.62	12.53
Decamethyl-cyclopentasiloxane	D5	C ₁₀ H ₃₀ O ₅ Si ₅	370.77	4.73
Dodecamethyl-cyclohexasiloxane	D6	C ₁₂ H ₃₆ O ₆ Si ₆	444.93	0.33
Trimethyl-silanol	TMS	C ₃ H ₁₀ OSi	90.20	-
Total (ppm-mol)				2.14

After purification, biomethane is compressed for injection in NG grids [21], while the removed CO₂ can be compressed and pipeline transported to oil fields as an enhanced oil recovery (EOR) agent generating revenue that compensates carbon capture and storage (CCS) costs [22]. Since the CO₂ source in the landfill is mostly biomass originated from photosynthesis, landfill-gas processing with the CO₂-to-EOR process creates bioenergy with CCS; i.e., a BECCS system [23]. BECCS systems combine carbon-neutral bioenergy generation with CCS in suitable geological formations [24], yielding negative CO₂ emissions and continuous net CO₂ drainage from the atmosphere [25].

1.1. Landfill-Gas Decarbonation: Advantages of Gas-Liquid Membrane Contactors

Different approaches of decarbonation technologies to convert landfill-gas into biomethane are compared, and gas-liquid membrane contactors' (GLMCs') advantages are presented to clarify why they are a feasible landfill-gas decarbonation technology.

Common separation technologies for landfill-gas decarbonation present some disadvantages. Firstly, pressure swing adsorption [26] entails a biomethane purity recovery tradeoff [21], and H₂S/water should be removed beforehand [2]. Moreover, the operation is intermittent due to adsorbent regeneration demanding control and maintenance. Sec-

only, packed-column chemical absorption [27] presents several hydraulic issues, such as foaming, flooding, entrainment, obligatory gravity alignment, etc. [28]. Thirdly, membrane-permeation [29] dismisses solvent handling and is gravity indifferent, modular, and recommended for high CO₂ fugacity streams [30]. In spite of this, membrane-permeation is limited by permeability-selectivity tradeoff [31] and entails compression costs to generate a driving force [32].

A different concept is the new technology known as gas–liquid membrane contactors (GLMCs), a hybrid of chemical absorption and membrane-permeation that combines the high selectivity of the former with the gravity indifference, modularity, phase segregation, and high transfer area of the latter, without the respective drawbacks [33]. Several positive attributes recommend GLMCs for landfill-gas decarbonation (and desulfurization), such as modularity, linear scale-up, independent control of flowrates [34], gravity indifference, no hydraulic issues, high CO₂/CH₄ selectivity entailing low CH₄ losses [35], and high transfer area per shell [36] due to the high packing density [37]. Compared to packed-column chemical absorption, GLMC size and weight reductions reach 70% and 66%, respectively [38]. GLMC design can prescribe gas (*V*) and solvent (*L*) flows in parallel (co-current) contact [39] or in countercurrent contact [40]. *V* can flow inside hollow-fiber membranes (HFMs) [41] or in the shell [42] and vice versa for *L*. GLMCs can also work as CO₂ strippers for solvent regeneration, albeit they would require a stripping gas in this case, such as nitrogen [43]. A complete description of GLMC principles can be found elsewhere [44].

1.2. GLMC Modeling for Landfill-Gas/Biogas Decarbonation

The literature presents several GLMC modeling approaches for gas decarbonation with varying simplifications. A common simplification involves zero pressure-drop and isothermal operation with feeds/products at the same temperature, as was shown in the one-dimensional (1D) mass balance of Teplyakov et al. [45]. Belaïssaoui et al. [46] also developed a simplified isothermal 1D mass transfer model for CO₂ physical absorption with pressurized water neglecting heat effects and pressure-drop. Belaïssaoui and Favre [47] used the same isothermal 1D mass transfer model with HFM-side and shell-side pressure-drop calculations via Hagen–Poiseuille and Happel equations, respectively. The common simplifying assumptions of Teplyakov et al. [45], Belaïssaoui et al. [46], and Belaïssaoui and Favre [47] correspond to neglect convective solvent-gas heat transfer and absorption/phase-change thermal effects, consequently overestimating CO₂ solubility in the solvent. Gas absorption is always exothermic, i.e., isothermal absorption is unrealistic. Moreover, in Teplyakov et al. [45], Belaïssaoui et al. [46], and Belaïssaoui and Favre [47], H₂O *L* → *V* transfer and phase-change thermal effects were also neglected. In a similar context, Fougerit et al. [48] approached isothermal 1D GLMC modeling using OpenFOAM software to investigate decarbonation of CO₂-CH₄ mixtures.

Li et al. [49] studied GLMC landfill-gas decarbonation with aqueous-Selexol solving the two-dimensional (2D) mass transfer partial differential equations via the finite element method with COMSOL software. However, ideal gas behavior was assumed for $P \geq 12$ bar and Selexol has high viscosity and is not recommended for GLMC HFMs. Previously, Li et al. [50] used aqueous K₂CO₃ for GLMC chemical absorption. Tantikhajongosol et al. [51] investigated simultaneous isothermal transfers of CO₂ (40 %mol) and H₂S (500 ppm-mol) to pressurized water using compressibility factors for real gas behavior. Nakhjiri and Heydarinasab [52] compared GLMC decarbonation performances of CO₂-CH₄ mixtures with aqueous ethylenediamine, aqueous-2-(1-piperazinyl)-ethylamine, and aqueous potassium sarcosinate. All these exothermic absorptions were simulated via COMSOL isothermal modeling assuming ideal gas behavior without pressure drops.

As shown above, typical literature GLMC models for landfill-gas/biogas decarbonation present one or more simplifications, such as (i) isothermal operation; (ii) ideal gas behavior at moderate/high pressures; (iii) negligible H₂O *L* → *V* transfer and solvent losses; (iv) negligible CH₄ *V* → *L* transfer; and (v) the Henry's law for CO₂ interfacial vapor–liquid

equilibrium (VLE). Such simplifications entail unrealistic results for industrial conditions. Isothermal operations may be valid only for some small-scale low-loading physical absorption. Moreover, bidirectional water transfer ($L \rightarrow V$ or $V \rightarrow L$) cannot be neglected since raw landfill-gas is usually water saturated and the solvent is aqueous [53]. Therefore, complete and thermodynamically rigorous GLMC modeling is rare in the literature. An example is presented by de Medeiros et al. [54] for high-pressure NG decarbonation with aqueous-monoethanolamine-methyldiethanolamine (aqueous-MEA-MDEA) adopting an acid-gas/water/MEA/MDEA reactive VLE [55] and assuming high-pressure V and L compressible flows with full thermodynamics via the Peng–Robinson equation-of-state (PR-EOS) and 1D V and L mass/energy/momentum balances [54].

Machine learning techniques typically use a large amount of data to train black-box models to perform reliable and realistic predictions [56]. In principle, these techniques could also be employed to predict GLMC CO_2 absorption [57] with aqueous solvents [58]. However, these models basically rely on a heavy load of information for extensive training in a statistical context and completely ignore mass/energy/momentum conservation and thermodynamics. Consequently, if not sufficiently trained over prohibitively extensive databases of initial/final temperatures/pressures/compositions, they can generate distorted predictions in deterministic processes totally driven by physical principles like distillation columns, heat exchangers, direct-contact columns, chemical reactors, and GLMC separations.

1.3. GLMC Modeling in Process Simulators

Simulation is an important tool for the analysis, monitoring, fault detection, troubleshooting, and design of chemical processes, as evaluations can be performed analytically with high precision, eliminating unnecessary time-consuming and costly experiments [59]. GLMC modeling for professional process simulators is important, because: (i) the model can take advantage of vast numbers of accurate thermodynamic/transport frameworks available in simulators; and (ii) the integration of a GLMC battery with the process flow-sheet is immediately performed in the simulator, accelerating industrial design, process analysis, and economic evaluations. Despite this, process simulator GLMC studies are scarce in the literature and still constitute relevant scientific challenges [60].

Hoff et al. [61] developed a GLMC model for flue gas and high-pressure NG decarbonation with mass/energy/momentum balances. The VLE was modeled via Henry's law with activity coefficients to account for liquid non-ideality. The model was validated with lab-scale experiments. Hoff and Svendsen [62] improved the previous thermodynamic model [61] to investigate the low-pressure decarbonation of offshore gas-turbine flue gas with the SINTEF/NTNU/CO2SIM simulator, and high-pressure NG decarbonation with the process simulator Protreat.

Quek et al. [63] studied high-pressure NG decarbonation with a 2D adiabatic GLMC CO_2 transfer model in gPROMS. Quek et al. [64] developed a more complete GLMC model for gPROMS admitting CO_2 transfer only, HFM pore-wetting prediction, PR-EOS gas behavior, water evaporation via Raoult's law, hydrocarbon loading via Henry's law, simplified energy balance, and no pressure drop. The model was validated against lab-scale and pilot-scale experiments. Quek et al. [65] employed the previous gPROMS model [64] for high-pressure NG decarbonation via the GLMC model evincing heat savings at the expense of inefficient CO_2 abatement.

Kerber and Repke [66] studied biogas purification with pressurized water and a flat-sheet membrane GLMC model, considering solvent evaporation and isothermal operation. Villeneuve et al. [67] developed an Aspen Modeler GLMC 1D adiabatic multicomponent transfer model for the comparison of GLMC and packed columns for NG decarbonation with aqueous ammonia considering ideal gas behavior and e-NRTL for the liquid phase. Villeneuve et al. [68] used an older [67] GLMC model to investigate the impact of water condensation on aqueous MEA NG decarbonation.

Usman et al. [69] studied high-pressure pre-combustion GLMC decarbonation using ionic-liquid 1-butyl-3-methylimidazolium tricyanomethanide with a MATLAB 1D transfer model based on resistance-in-series approaches. Posteriorly Usman et al. [70] integrated the MATLAB code with an Aspen-HYSYS simulator via Cape-Open resources, retaining isothermal behavior and Henry's law VLEs.

Recently, McQuillan et al. [71] developed a one-dimensional distributed GLMC model for the Aspen Custom Modeler to evaluate potassium glycinate as a solvent for direct air capture, but the model presents simplifications, such as isothermal modeling, Henry's law VLE, no energy balances, and no pressure-drop calculation.

A more efficient way to develop new unit operation models while maintaining access to Aspen-HYSYS rigorous thermodynamic resources is by creating HYSYS unit operation extensions (UOEs) [72]. However, the literature lacks works on GLMC HYSYS modeling, but there are exceptions for CO₂-rich NG high-pressure CO₂ removal. In da Cunha et al.'s study [73], a GLMC-UOE-1 considered just CO₂ transfer, without energy balances and pressure-drop calculations. Posteriorly, da Cunha et al. [74] developed a more complete GLMC-UOE model with multicomponent bidirectional transfer and mass/energy/momentum balances for gas and solvent flows, provided on an HYSYS thermodynamic basis. This study was conducted in offshore high-pressure conditions for the decarbonation of CO₂-rich NG via GLMC with aqueous-amines. However, since landfill-gas decarbonation occurs under milder conditions, the literature lacks a specific GLMC-UOE model developed for its specific hydrodynamic conditions.

1.4. Siloxane Removal from Landfill-Gas: The Advantages of Selexol Absorption

Several studies on landfill-gas sweetening consider pressurized-water absorption, but it was shown [75] that water absorption is inefficient for siloxane removal. Lântelä et al. [76] studied landfill-gas sweetening in a water-absorption column evincing a 16.6% efficiency of siloxane removal as follows: TMS/D5 was significantly removed, while L2/L3/D3 was enriched, and L4/L5/D4 remained invariant.

The literature indicates Dimethyl-Ether-Polyethylene-Glycol (DEPG)—Selexol—as a promising siloxane absorbent from landfill-gas, with successful applications [75]. Ryckebosch et al. [77] suggest DEPG also for CO₂/H₂S removal from landfill-gas, as is performed for synthesis-gas purification [78]. However, DEPG absorption is an expensive technology, i.e., it is not advisable to use DEPG absorption for full landfill-gas purification. Belaïssaoui and Favre [47] suggest siloxane and H₂S DEPG removal prior to landfill-gas decarbonation with water. However, in this case, the higher H₂S content will unnecessarily compete with trace siloxanes. Moreover, Faiz et al. [79] already proved pressurized-water reliability for H₂S removal and Li et al. [80] approved pressurized-water packed columns for biogas decarbonation and suggested its replacement by GLMC.

Given these facts, and since landfill-gas is similar to biogas, the present work proposes a new landfill-gas-to-biomethane route; namely: GLMC CO₂/H₂S removal with pressurized water, followed by siloxane removal via a finishing DEPG-absorption column requiring a low DEPG circulation rate. GLMC CO₂/H₂S water absorption and siloxane DEPG absorption are both modeled via the HYSYS Acid-Gas Physical-Solvents Thermodynamic Package based on the PC-SAFT equation-of-state [81].

1.5. The Present Work

As shown in Section 1.2, the literature presents recent studies on GLMC modeling for landfill-gas decarbonation, but all bear modeling deficiencies or scope limitations. Moreover, process simulation GLMC studies are still scarce (Section 1.3). A remarkable literature gap is the absence of complete GLMC models with multicomponent mass/energy/momentum balances, sustained by an adequate thermodynamic framework for vapor-liquid equilibrium and reliable predictions of thermodynamic/transport properties.

The present work discloses a novel GLMC HYSYS unit operation extension—GLMC-UOE—developed for the steady-state simulation of multicomponent bidirectional ($V \rightarrow L$, $L \rightarrow V$) mass/heat transmembrane transfers using a fugacity-difference driving force, rigorous VLE, and thermodynamic modeling via the HYSYS Acid-Gas Physical-Solvents Package and rigorous energy balances taking into account chemical/phase-change/compressibility temperature effects, pressure drops, and non-isothermal operations. GLMC-UOE-simulated $\text{CO}_2/\text{H}_2\text{S}$ removal from landfill-gas with pressurized water and can handle GLMC countercurrent and parallel contacts generating composition/temperature/pressure profiles. It is demonstrated that the new HYSYS-based contactor model can be validated with bench-scale literature data and used in industrial-scale batteries with the same module hydrodynamics. Moreover, once calibrated, the model becomes economically valuable since it can: (i) predict the performance of industrial contactor batteries under scale-up/scale-down conditions; (ii) detect process faults, membrane leakages, and wetting; and (iii) be used for process troubleshooting.

The literature presents several incomplete landfill-gas/biogas purification studies, as most of them ignore H_2S and siloxane removal and/or $\text{CH}_4/\text{H}_2\text{O}$ bidirectional transfers and/or temperature/pressure changes. In addition, the proposed landfill-gas-to-biomethane route adopts novel intensified operations to reduce space requirements and to improve energy efficiency. As shown in Section 1.4, the selection of an adequate solvent for siloxane removal is a critical step for biomethane specification. Since Selexol is considered efficient, albeit expensive, this process proposes CO_2 and H_2S removal prior to Selexol absorption for siloxane removal, to reduce the amount of Selexol required. This work proved that Selexol absorption is a promising choice for siloxane removal.

In summary, a novel and complete waste-to-energy landfill-gas-to-biomethane process was solved in Aspen-HYSYS 10.0 considering: (i) an intensified non-isothermal GLMC battery with pressurized water ($T = 15\text{ }^\circ\text{C}$, $P = 7\text{ bar}$) for $\text{CO}_2/\text{H}_2\text{S}$ removal with $\text{CO}_2/\text{H}_2\text{S}/\text{CH}_4/\text{H}_2\text{O}$ bidirectional transmembrane transfers and heat effect predictions; (ii) intensified $\text{CO}_2/\text{H}_2\text{S}$ stripping at $P = 30\text{ bar}$, reducing costs for CO_2 -to-EOR ($P = 300\text{ bar}$) compression; and (iii) multicomponent siloxane removal using a DEPG absorption ($T = 15\text{ }^\circ\text{C}$, $P = 7\text{ bar}$) column.

2. Methods

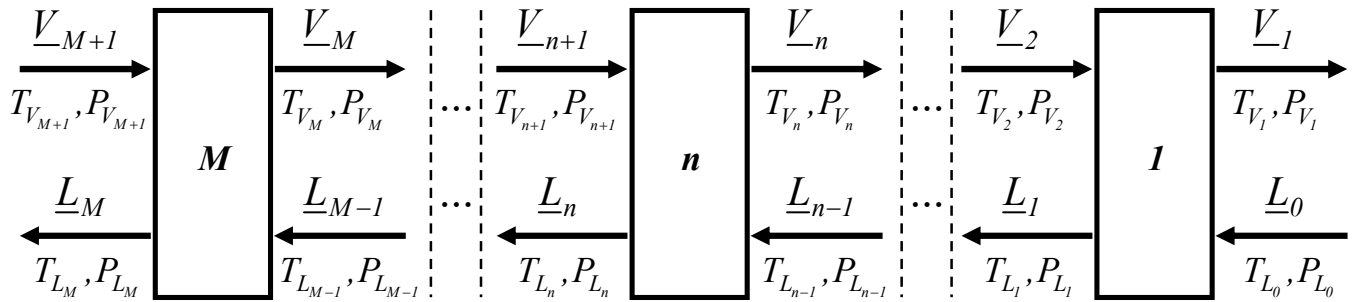
GLMC-UOE modeling and the landfill-gas-to-biomethane process are addressed.

2.1. GLMC-UOE Development

GLMC-UOE was created using Visual-Basic 6.0 with the embedded HYSYS-Type Library that offers runtime commands to access HYSYS. An external dynamic link library (DLL) file was generated by code compilation. An extension definition file (EDF) was also developed with the Aspen-HYSYS Extension View Editor for DLL linkage to HYSYS and to create user-interface windows for setting GLMC conditions during the simulations in HYSYS PFD. After registering the extension, GLMC-UOE becomes available in a model palette and can access all HYSYS stream/property calculation resources.

GLMC-UOE considers 1D steady-state L and V axial flows for the simulation of GLMC batteries of N_M paralleled modules. After being entered into the GLMC module, both L and V can become two-phase. There are two models for different L/V contacts: (i) the countercurrent-contact distributed GLMC model (GLMC-CCC-D); and (ii) parallel-contact (co-current) distributed GLMC model (GLMC-PC-D). Both models are built for landfill-gas decarbonation/desulfurization with physical-solvent pressurized water and involve axially discretizing a GLMC module as a succession of M elements in Figure 1a,b, where the countercurrent V/L streams (arrows) are valid for GLMC-CCC-D (Figure 1a) and the parallel V/L streams for GLMC-PC-D (Figure 1b).

(a) Countercurrent GLMC Module as a Cascade of M ($M \geq 1$) GLMC Elements



(b) Parallel GLMC Module as a Cascade of M ($M \geq 1$) GLMC Elements

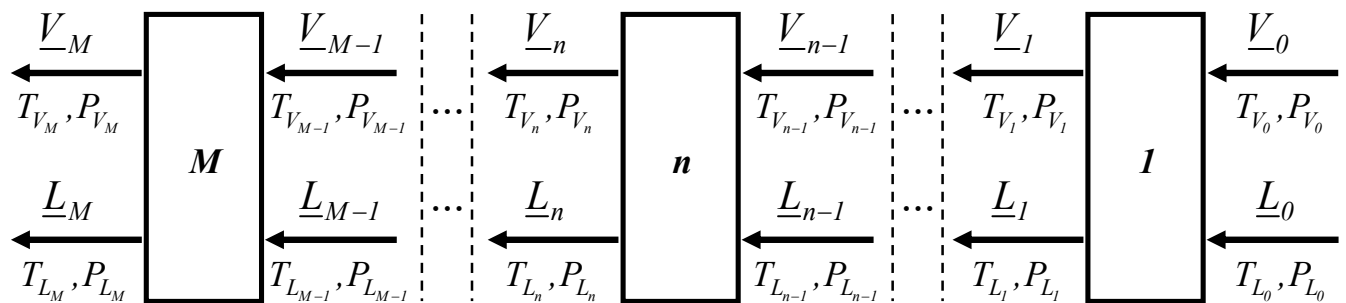


Figure 1. Representations of countercurrent and parallel GLMC modules as cascades of M elements (streams are numbered by the origin element). GLMC battery feed data: (a) $L_0, V_{M+1}, T_{L_0}, T_{V_{M+1}}, P_{L_0}, P_{V_{M+1}}$ (GLMC-CCC-D) and (b) $L_0, V_0, T_{L_0}, T_{V_0}, P_{L_0}, P_{V_0}$ (GLMC-PC-D).

Besides the aforesaid concepts, GLMC distributed model assumptions comprise: (i) L/V countercurrent or parallel contacts; (ii) V on the HFM side and L on the shell side; (iii) 1D axial two-phase plug flow for L/V mass/energy/momentum balances; (iv) rigorous VLEs and thermodynamic and transport property calculations via the Aspen-HYSYS Acid-Gas Physical-Solvents Package (PC-SAFT equation-of-state); (v) multicomponent system with $\text{CO}_2/\text{CH}_4/\text{H}_2\text{S}/\text{H}_2\text{O}$ and the siloxanes in Table 1 (except L3/L5/TMS; number of components $nc = 11$), where $\text{CO}_2/\text{CH}_4/\text{H}_2\text{S}/\text{H}_2\text{O}$ are the only species for which bidirectional transfers ($V \rightarrow L, L \rightarrow V$) are considered, since siloxanes are heavy species that practically do not transfer to water; (vi) L/V pressure drop; (vii) L/V outlet composition/temperature/pressure calculations; (viii) adiabatic GLMC modules (external heat transfer coefficient $U_E = 0$) with convective transmembrane heat transfer (internal heat transfer coefficient $U_I \neq 0$); (ix) L/V absorption/compressibility/phase-change heat effects; (x) distributed transmembrane heat and species transfer model using respective driving forces log-mean temperature difference and log-mean species fugacity differences; (xi) direction of positive heat/mass transfers: $V \rightarrow L$; (xii) countercurrent GLMC module with discretization as a cascade of M small countercurrent GLMC elements (Figure 1a) solved with simultaneous corrections [82] Newton–Raphson iterations; (xiii) parallel GLMC module discretized as a cascade of M small parallel GLMC elements (Figure 1b) sequentially solved via element Newton–Raphson iterations; and (xiv) GLMC dependent variables are $nc \times 1$ vectors $\underline{L}_n, \underline{V}_n$ of component flowrates (mol/s) that leave element n ($n = 1 \dots M$) (for the entire battery) as well as the temperatures/pressures $\underline{L}_n, \underline{V}_n, T_{L_n}, T_{V_n}, P_{L_n}, P_{V_n}$ ($n = 1 \dots M$). Interfacial heat and mass transfer fluxes for each element were eliminated from the phenomenological relationships in terms of driving forces. The specifications were battery size, GLMC module geometry, and the two $nc \times 1$ vectors of component feeds (mol/s) and their temperatures/pressures, $\underline{L}_0, \underline{V}_{M+1}, T_{L_0}, T_{V_{M+1}}, P_{L_0}, P_{V_{M+1}}$ for GLMC-CCC-D, and $\underline{L}_0, \underline{V}_0, T_{L_0}, T_{V_0}, P_{L_0}, P_{V_0}$ for GLMC-PC-D.

2.1.1. Element Mass Balances

For each GLMC element, n ($n = 1 \dots M$), the transmembrane mass transfer of species k ($k = 1 \dots nc$) was calculated with the log-mean differences of species k fugacities ($\Delta \hat{f}_{k,n}^{LM}$, bar) as the driving force [73] (asymptotically correct as M increases). Supposed constant, the transmembrane species mass transfer coefficients (Π_k , mol/(s.bar.m²), $k = 1 \dots nc$) were calibrated to adjust transmembrane mass transfer rates for element n ($N_{k,n}$, mol/s) as performed by de Medeiros et al. [54], except for the non-transferable siloxanes, where $\Pi_k = 0$, $N_{k,n} = 0$. The GLMC module heat/mass transfer area was A_{GLMC} , while the element transfer area was A_{GLMC}/M . Thus, the single-module separation capacity was pre-defined [44]. In order to determined separation targets, the battery transfer area can be increased (or decreased) with the increase (or decrease) in N_M in the GLMC-UOE parameter window. The calibration of mass transfer coefficients, Π_k , consists of adjusting CO₂/CH₄/H₂S/H₂O transmembrane transfers with GLMC experimental data (Appendices A–D), as in da Cunha et al. [74]. The set of transferable species is $\{TS\} \equiv \{CO_2, CH_4, H_2S, H_2O\}$. Set $\{TS^+\}$ contains species with $N_{k,n} > 0$ ($V \rightarrow L$ transfer), while set $\{TS^-\}$ contains those with $N_{k,n} < 0$ ($L \rightarrow V$ transfer), i.e., $\{TS\} = \{TS^+\} \cup \{TS^-\}$. The transference direction of a transferable component has to be updated for the elements in the axial direction, so that for $k \in \{TS\}$, $\hat{f}_{k,n}^V > \hat{f}_{k,n}^L \Rightarrow k \in \{TS^+\}$; otherwise, $k \in \{TS^-\}$. In the landfill-gas context, normally $\{TS^+\} = \{CO_2, H_2S, CH_4\}$ and $\{TS^-\} = \{H_2O\}$. The model does not take into account membrane pore wetting directly, i.e., pore wetting is superseded by the calibration of Π_k , $k \in \{TS\}$ by combining GLMC-UOE with experimental GLMC data. Once calibrated, Π_k , $k \in \{TS\}$ can be supposed as invariant to relatively small changes in design and/or hydrodynamics. Moreover, calibrated Π_k , $k \in \{TS\}$ is invariant for greater (lower) V values with a constant V/L ratio and the same feed temperature/pressure and module geometry, where the module number, N_M , increases or decreases proportionally to V in order to maintain module hydrodynamics [74].

Equations (1a)–(1d) and (2a)–(2c) represent the multicomponent mass balances in element n ($n = 1 \dots M$), where Equations (1c) and (2a) apply to GLMC-CCC-D and Equations (1d) and (2b) for GLMC-PC-D, and $\hat{f}_{k,n}^V, \hat{f}_{k,n}^L$ are species k respective fugacities (bar) in V/L streams that leave n . In Equations (1a)–(2c), the species transfer rates ($N_{k,n}$, mol/s) are eliminated using the right-hand sides of Equations (1a)–(1d). Consequently, the mass balances reduce to $2nc$ element equations presented in Equations (2a) (or (2b)) and (2c). Equation (3) represents the resulting $2nc \times 1$ vector of mass balances for element n (in GLMC-CCC-D or GLMC-PC-D), whose dependent variables are the element $2nc + 4$ outlet variables ($L_n, V_n, T_{L,n}, T_{V,n}, P_{L,n}, P_{V,n}$) [82].

$$N_{k,n} = \Pi_k (N_M A_{GLMC} / M) \Delta \hat{f}_{k,n}^{LM} \quad (k \in \{TS\}, n = 1 \dots M) \quad (1a)$$

$$N_{k,n} = 0 \quad (k \notin \{TS\}, n = 1 \dots M) \quad (1b)$$

$$\Delta \hat{f}_{k,n}^{LM} = \frac{(\hat{f}_{k,n}^V - \hat{f}_{k,n-1}^L) - (\hat{f}_{k,n+1}^V - \hat{f}_{k,n}^L)}{\ln(\hat{f}_{k,n}^V - \hat{f}_{k,n-1}^L) - \ln(\hat{f}_{k,n+1}^V - \hat{f}_{k,n}^L)} \quad (k \in \{TS\}, n = 1 \dots M, GLMC - CCC - D) \quad (1c)$$

$$\Delta \hat{f}_{k,n}^{LM} = \frac{(\hat{f}_{k,n-1}^V - \hat{f}_{k,n-1}^L) - (\hat{f}_{k,n}^V - \hat{f}_{k,n}^L)}{\ln(\hat{f}_{k,n-1}^V - \hat{f}_{k,n-1}^L) - \ln(\hat{f}_{k,n}^V - \hat{f}_{k,n}^L)} \quad (k \in \{TS\}, n = 1 \dots M, GLMC - PC - D) \quad (1d)$$

$$V_{k,n} + N_{k,n} - V_{k,n+1} = 0 \quad (k = 1 \dots nc, n = 1 \dots M, GLMC - CCC - D) \quad (2a)$$

$$V_{k,n} + N_{k,n} - V_{k,n-1} = 0 \quad (k = 1 \dots nc, n = 1 \dots M, GLMC - PC - D) \quad (2b)$$

$$L_{k,n-1} + N_{k,n} - L_{k,n} = 0 \quad (k = 1 \dots nc, n = 1 \dots M) \quad (2c)$$

$$\underline{E}_n^{MB} = \underline{0} \quad (n = 1 \dots M) \quad (3)$$

2.1.2. Element Energy Balances

$V \rightarrow L$ is the positive transfer direction, as previously stated. For element n ($n = 1 \dots M$), energy balances are presented for V/L streams—of the entire battery—considering the energy transport of V/L inlet/outlet streams, transmembrane convective heat transfer, and the transmembrane energy transfer coupled to the transfer of species k presented by the species k transfer rate in element n times k partial molar enthalpy at origin. The V/L partial molar enthalpies (kJ/mol) of k at origin in element n , $\langle \bar{H}_{k,n}^V \rangle$, $\langle \bar{H}_{k,n}^L \rangle$, are approximated by the arithmetic means of respective inlet/outlet partial molar enthalpies ($\langle \bar{H}_{k,n}^V \rangle = (\bar{H}_{k,n+1}^V + \bar{H}_{k,n}^V)/2$ for GLMC-CCC-D, $\langle \bar{H}_{k,n}^V \rangle = (\bar{H}_{k,n-1}^V + \bar{H}_{k,n}^V)/2$ for GLMC-PC-D, and $\langle \bar{H}_{k,n}^L \rangle = (\bar{H}_{k,n-1}^L + \bar{H}_{k,n}^L)/2$), which becomes asymptotically correct as $M \rightarrow \infty$. V energy balance is expressed via Equation (5a) for GLMC-CCC-D and via Equation (5b) for GLMC-PC-D, while L energy balance is expressed via Equation (5c) for GLMC-CCC-D and via Equation (5d) for GLMC-PC-D, where \bar{H}_{V_n} , \bar{H}_{L_n} (kJ/mol) are V/L molar enthalpies leaving element n , and $\underline{1}$ is an $nc \times 1$ vector of ones. Since, partial molar enthalpies are not available in the HYSYS (only molar enthalpies are), they have to be calculated via Equations (4a) and (4b) using mole fraction (Y_k, X_k) derivatives of molar enthalpies numerically generated with finite differences, as in da Cunha et al. [74].

$$\bar{H}_k^V = \bar{H}_V - \sum_{i=1}^{nc} \left(\frac{\partial \bar{H}_V}{\partial Y_i} \right)_{T,P,Y_j \neq i} + \left(\frac{\partial \bar{H}_V}{\partial Y_k} \right)_{T,P,Y_j \neq k} \quad (Y_k = V_k / \underline{1}^T \underline{V}) \quad (4a)$$

$$\bar{H}_k^L = \bar{H}_L - \sum_{i=1}^{nc} \left(\frac{\partial \bar{H}_L}{\partial X_i} \right)_{T,P,X_j \neq i} + \left(\frac{\partial \bar{H}_L}{\partial X_k} \right)_{T,P,X_j \neq k} \quad (X_k = L_k / \underline{1}^T \underline{L}) \quad (4b)$$

Element n transmembrane heat transfer is presented with the transmembrane log-mean temperature difference for element n (ΔT_n^{LM} in Equation (6a) for GLMC-CCC-D, or in Equation (6b) for GLMC-PC-D, also asymptotically correct as $M \rightarrow \infty$), the internal heat transfer coefficient U_I (kW/m².K), and $N_{MA} A_{GLMC} / M$ the element n battery internal transfer area. For GLMC-CCC-D [74], Equation (6a) is substituted in Equations (5a) and (5c), reducing the energy-balance equations of element n to only Equations (5a) and (5c). Analogously, for GLMC-PC-D [54], Equation (6b) is substituted in Equations (5b) and (5d). In both cases, the resulting 2×1 vector of element n energy balances is written as $\underline{F}_n^{EB} = \underline{0}$ in Equation (7). The $2nc + 4$ outlet variables of element n ($\underline{L}_n, \underline{V}_n, T_{L_n}, T_{V_n}, P_{L_n}, P_{V_n}$) are the dependent variables of $\underline{F}_n^{EB} = \underline{0}$.

$$(\underline{1}^T \underline{V}_{n+1}) \bar{H}_{V_{n+1}} - (\underline{1}^T \underline{V}_n) \bar{H}_{V_n} - \sum_{k \in \{TS^+\}} N_k \left(\frac{\bar{H}_{k,n+1}^V + \bar{H}_{k,n}^V}{2} \right) - \sum_{k \in \{TS^-\}} N_k \left(\frac{\bar{H}_{k,n-1}^L + \bar{H}_{k,n}^L}{2} \right) - \frac{U_I N_{MA} A_{GLMC} \Delta T_n^{LM}}{M} = 0 \quad (5a)$$

$$(\underline{1}^T \underline{V}_{n-1}) \bar{H}_{V_{n-1}} - (\underline{1}^T \underline{V}_n) \bar{H}_{V_n} - \sum_{k \in \{TS^+\}} N_k \left(\frac{\bar{H}_{k,n-1}^V + \bar{H}_{k,n}^V}{2} \right) - \sum_{k \in \{TS^-\}} N_k \left(\frac{\bar{H}_{k,n-1}^L + \bar{H}_{k,n}^L}{2} \right) - \frac{U_I N_{MA} A_{GLMC} \Delta T_n^{LM}}{M} = 0 \quad (5b)$$

$$(\underline{1}^T \underline{L}_{n-1}) \bar{H}_{L_{n-1}} - (\underline{1}^T \underline{L}_n) \bar{H}_{L_n} + \sum_{k \in \{TS^+\}} N_k \left(\frac{\bar{H}_{k,n+1}^V + \bar{H}_{k,n}^V}{2} \right) + \sum_{k \in \{TS^-\}} N_k \left(\frac{\bar{H}_{k,n-1}^L + \bar{H}_{k,n}^L}{2} \right) + \frac{U_I N_{MA} A_{GLMC} \Delta T_n^{LM}}{M} = 0 \quad (5c)$$

$$(\underline{1}^T \underline{L}_{n-1}) \bar{H}_{L_{n-1}} - (\underline{1}^T \underline{L}_n) \bar{H}_{L_n} + \sum_{k \in \{TS^+\}} N_k \left(\frac{\bar{H}_{k,n-1}^V + \bar{H}_{k,n}^V}{2} \right) + \sum_{k \in \{TS^-\}} N_k \left(\frac{\bar{H}_{k,n-1}^L + \bar{H}_{k,n}^L}{2} \right) + \frac{U_I N_{MA} A_{GLMC} \Delta T_n^{LM}}{M} = 0 \quad (5d)$$

$$\Delta T_n^{LM} = \frac{(T_{V_n} - T_{L_{n-1}}) - (T_{V_{n+1}} - T_{L_n})}{\ln(T_{V_n} - T_{L_{n-1}}) - \ln(T_{V_{n+1}} - T_{L_n})} \quad (GLMC - CCC - D) \quad (6a)$$

$$\Delta T_n^{LM} = \frac{(T_{V_n} - T_{L_n}) - (T_{V_{n-1}} - T_{L_{n-1}})}{\ln(T_{V_n} - T_{L_n}) - \ln(T_{V_{n-1}} - T_{L_{n-1}})} \quad (GLMC - PC - D) \quad (6b)$$

$$\underline{F}_n^{EB} = \underline{0} \quad (n = 1 \dots M) \quad (7)$$

2.1.3. Element Pressure Drop

The element n pressure-drop calculation aims at determining its outlet pressures P_{L_n}, P_{V_n} . To calculate hydraulic diameters and flow-section areas, HFMs are perceived as rigid with external and internal diameters, d_o, d_i . The HFM bundle is distributed with HFM centers on an equilateral triangular lattice in a GLMC shell (Figure 2). Hence, the center-center distance, p_{HF} , of adjacent HFMs is constant, and S_{FREE} defines in each triangle the free flow area. In Figure 2a, simple reasoning shows that the number of triangles (N_{TRI}) is asymptotically presented in Equation (8) for N_{HF} HFMs per shell. Since the entire shell transversal section (diameter D) is covered by the triangular lattice without triangle superposition, Equation (9) and Equation (10), respectively, hold for p_{HF} and S_{FREE} . With A_{CSS} (m^2) as the shell-side flow section in Equation (11)—which asymptotically ($N_{HF} \rightarrow \infty$) equals $N_{TRI} * S_{FREE}$ —and with HP_S as the shell-side hydraulic perimeter, one can see that the shell-side hydraulic diameter, d_{HS} (m), in the second term of Equation (12) is also the hydraulic diameter for S_{FREE} in the last term of Equation (12).

$$N_{TRI} = 2N_{HF} - 2\sqrt{N_{HF}} \quad (8)$$

$$N_{TRI} \frac{\sqrt{3}}{4} p_{HF}^2 = \frac{\pi D^2}{4} \Rightarrow p_{HF} = \sqrt{\frac{\pi D^2 / 4}{(\sqrt{3}/2)(N_{HF} - \sqrt{N_{HF}})}} \quad (9)$$

$$S_{FREE} = \frac{\sqrt{3}}{4} p_{HF}^2 - (1/2) \frac{\pi d_o^2}{4} \quad (10)$$

$$A_{CSS} = \frac{\pi D^2}{4} - N_{HF} \frac{\pi d_o^2}{4} \quad (11)$$

$$d_{HS} = \frac{4A_{CSS}}{HP_S} = \frac{4S_{FREE}}{\pi d_o / 2} = d_o \left(\frac{2\sqrt{3}}{\pi} \left(\frac{p_{HF}}{d_o} \right)^2 - 1 \right) \quad (12)$$

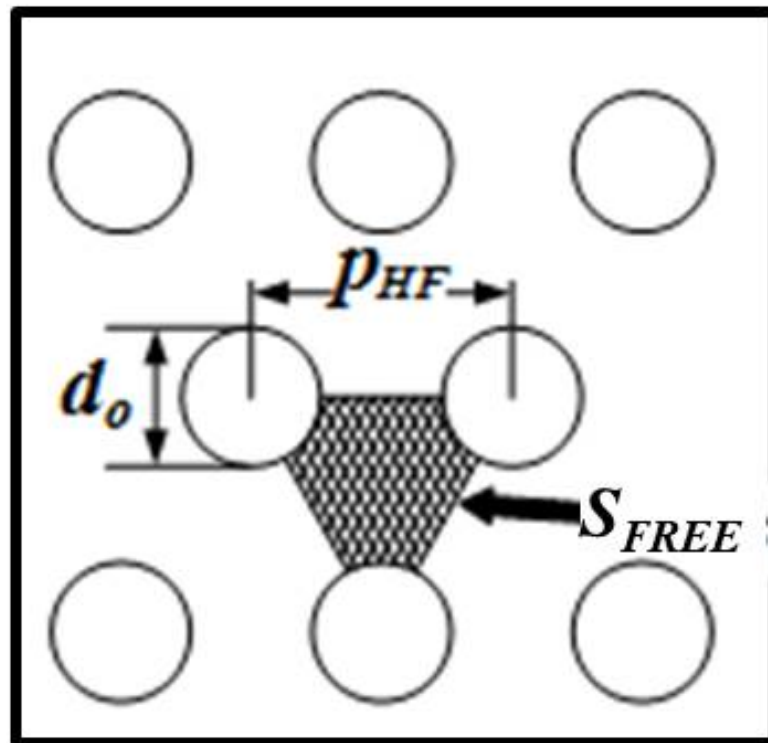


Figure 2. HFM bundle as equilateral triangular lattice (edge p_{HF}): triangle-free area, S_{FREE} , for shell-side liquid flow.

Equation (13) presents the HFM-side hydraulic diameter, d_{HHF} (m), while HFM-side flow-section A_{CSHF} (m²) and HFM outlet gas velocity v_{V_n} (m/s) of element n , with $\bar{\rho}_{V_n}$ (mol/m³) as the gas molar density, follow in Equation (14) and Equation (15), respectively. The HFM-side pressure-drop (head-loss) for element n , $h_{V_n}^{HF}$ (Pa), is presented by the Hagen–Poiseuille equation in Equation (16a) for GLMC-CCC-D and in Equation (16b) for GLMC-PC-D, where the property inlet/outlet arithmetic means are used and Z_M (m) is the module length. The shell-side pressure-drop across element n , $h_{L_n}^S$ (Pa), is calculated via the Happel equation (Equation (17)) with the support of Equation (18), Equation (19), and Equation (20), respectively determining the Kozeny factor, κ [83], the outlet liquid velocity, v_{L_n} , and the packing ratio, φ [83], where $\bar{\rho}_{L_n}$ (mol/m³) represents the outlet L mol density. Dynamic viscosities μ_V, μ_L in Equations (16a), (16b), and (17) are approximated by the viscosity of the predominant phase (gas for V and liquid for L), since V and L streams can become (or not) two phase at an axial position in the GLMC. The GLMC outlet V/L absolute pressures of element n , P_{V_n}, P_{L_n} (bar), are calculated via Equation (21a) for GLMC-CCC-D, Equation (21b) for GLMC-PC-D, and Equation (22).

$$d_{HHF} = d_i \quad (13)$$

$$A_{CSHF} = N_{HF} \pi d_i^2 / 4 \quad (14)$$

$$v_{V_n} = \frac{\underline{1}^T \underline{V}_n}{\bar{\rho}_{V_n} N_M A_{CSHF}} \quad (15)$$

$$h_{V_n}^{HF} = \frac{32(Z_M/M)}{d_{HHF}^2} \left(\frac{v_{V_{n+1}} + v_{V_n}}{2} \right) \left(\frac{\mu_{V_{n+1}} + \mu_{V_n}}{2} \right) \quad (GLMC - CCC - D) \quad (16a)$$

$$h_{V_n}^{HF} = \frac{32(Z_M/M)}{d_{HHF}^2} \left(\frac{v_{V_{n-1}} + v_{V_n}}{2} \right) \left(\frac{\mu_{V_{n-1}} + \mu_{V_n}}{2} \right) \quad (GLMC - PC - D) \quad (16b)$$

$$h_{L_n}^S = \frac{16\kappa(Z_M/M)}{d_{HS}^2} \left(\frac{\mu_{L_{n-1}} + \mu_{L_n}}{2} \right) \left(\frac{v_{L_{n-1}} + v_{L_n}}{2} \right) \frac{(\varphi)^2}{(1 - \varphi)^2} \quad (17)$$

$$\kappa = 150\varphi^4 - 314.44\varphi^3 + 241.67\varphi^2 - 83.039\varphi + 15.97 \quad (18)$$

$$v_{L_n} = \frac{\underline{1}^T \underline{L}_n}{\bar{\rho}_{L_n} N_M A_{CSS}} \quad (19)$$

$$\varphi = N_{HF} d_o^2 / D^2 \quad (20)$$

$$P_{V_{n+1}} - P_{V_n} - 10^{-5} h_{V_n}^{HF} = 0 \quad (GLMC - CCC - D) \quad (21a)$$

$$P_{V_{n-1}} - P_{V_n} - 10^{-5} h_{V_n}^{HF} = 0 \quad (GLMC - PC - D) \quad (21b)$$

$$P_{L_{n-1}} - P_{L_n} - 10^{-5} h_{L_n}^S = 0 \quad (22)$$

Equations (8)–(16a) and (16b) can be substituted into Equation (21a) for GLMC-CCC-D or into Equation (21b) for GLMC-PC-D, and Equations (17)–(20) can be substituted into Equation (22), so that the set of pressure-drop equations is reduced to Equations (21a) or (21b) and Equation (22). For element n , the final 2×1 vector of pressure-drop equations is expressed by Equation (23). Dependent variables of \underline{F}_n^{PD} are the $2nc + 4$ outlet variables $\underline{L}_n, \underline{V}_n, T_{L_n}, T_{V_n}, P_{L_n}, P_{V_n}$ of element n .

$$\underline{F}_n^{PD} = \underline{0} \quad (23)$$

For element n , the vector $\underline{\eta}_n$ of $2nc + 4$ dependent variables and the vector \underline{R}_n of $2nc + 4$ independent equation residues—either for GLMC-CCC-D or for GLMC-PC-D—are presented in Equation (24) for $n = 1, \dots, M$. Equation (25) represents the complete vector of $(2nc + 4) * M$ GLMC dependent variables ($\underline{\eta}$) and the complete vector of $(2nc + 4) * M$ GLMC residues (\underline{R}).

$$\underline{\eta}_n = \begin{bmatrix} L_n \\ T_{L_n} \\ P_{L_n} \\ V_n \\ T_{V_n} \\ P_{V_n} \end{bmatrix}, \quad \underline{R}_n = \begin{bmatrix} F_n^{MB} \\ F_n^{EB} \\ F_n^{PD} \end{bmatrix} = \underline{0} \quad (n = 1 \dots M) \quad (24)$$

$$\underline{R}(\underline{\eta}) = \begin{bmatrix} R_1 \\ R_2 \\ \vdots \\ R_M \end{bmatrix} = \underline{0}, \quad \underline{\eta} = \begin{bmatrix} \eta_1 \\ \eta_2 \\ \vdots \\ \eta_M \end{bmatrix} \quad (25)$$

2.1.4. Algorithm to Solve the Countercurrent GLMC Model (GLMC-CCC-D)

The GLMC-CCC-D system of $(2nc + 4)*M$ residues is solved for the $(2nc + 4)*M$ variables in Equation (25) using a cascade Newton–Raphson method known as the simultaneous corrections method [82] originally developed for countercurrent multistage cascades [74]. In this method, iterations occur simultaneously over all elements in order to solve Equations (24) and (25) until convergence. This rather involved and rigorous method will be used to solve GLMC-CCC-D for CO₂/H₂S removal from landfill-gas using partially analytical and partially numerical Jacobian matrices. It was developed elsewhere [74] and will not be further explained here. Figure 3 presents an algorithm flowchart for solving countercurrent-contact GLMCs (GLMC-CCC-D) (Figure 3a).

2.1.5. Algorithm to Solve the Parallel-Contact GLMC (GLMC-PC-D)

Despite the fact that the system in Equation (24) seems to be the same for GLMC-CCC-D and GLMC-PC-D models, the truth is that there are important differences between them because GLMC-CCC-D is a boundary value problem, while GLMC-PC-D is an initial value problem, which means that the GLMC-PC-D elements can be sequentially solved. As shown by da Cunha et al. [74], to solve GLMC-CCC-D, Newton–Raphson iterations throughout the entire cascade are necessary, while to solve GLMC-PC-D, it is only necessary to conduct Newton–Raphson iterations to solve Equation (24) until convergence for each element, n , sequentially starting from element 1 and terminating at element M . The algorithm for GLMC-PC-D is shown in Equation (26). Figure 3 presents a flowchart of the algorithm for solving a parallel-contact GLMC (GLMC-PC-D) (Figure 3b).

$$\left\{ \begin{array}{l} \text{Enter Feed Data : } L_0, V_0, T_{L_0}, T_{V_0}, P_{L_0}, P_{V_0} \\ \text{Create Initial Estimate for } \underline{\eta}_1 : \underline{\eta}_1^{(0)} \text{ (e.g., } \underline{\eta}_1^{(0)} = [L_0 \ T_{L_0} \ P_{L_0} \ V_0 \ T_{V_0} \ P_{V_0}]^T) \\ \text{For } n = 1 \rightarrow M \\ \quad \text{With } \underline{\eta}_n^{(0)} \text{ Solve } \underline{R}_n = \underline{0} \text{ for } \underline{\eta}_n \text{ via Newton – Raphson Method} \\ \quad \text{If } n < M \text{ Create Initial Estimate for } \underline{\eta}_{n+1} : \underline{\eta}_{n+1}^{(0)} \text{ (e.g., } \underline{\eta}_{n+1}^{(0)} = \underline{\eta}_n) \\ \text{End} \end{array} \right. \quad (26)$$

Since GLMC-PC-D elements are small parallel-contact contactors, the elements' logarithmic mean driving forces, Equations (1d) and (6b), are asymptotically equal to more palatable arithmetic mean driving forces, Equation (27a) and Equation (27b), respectively. That is, Equations (27a) and (27b) can replace Equations (1d) and (6b), respectively.

$$\Delta \hat{f}_{k,n}^{LM} = \frac{(\hat{f}_{k,n-1}^V - \hat{f}_{k,n-1}^L) + (\hat{f}_{k,n}^V - \hat{f}_{k,n}^L)}{2} \quad (k \in \{TS\}, n = 1 \dots M, \text{ GLMC - PC - D}) \quad (27a)$$

$$\Delta T_n^{LM} = \frac{(T_{V_n} - T_{L_n}) + (T_{V_{n-1}} - T_{L_{n-1}})}{2} \quad (n = 1 \dots M, \text{ GLMC - PC - D}) \quad (27b)$$

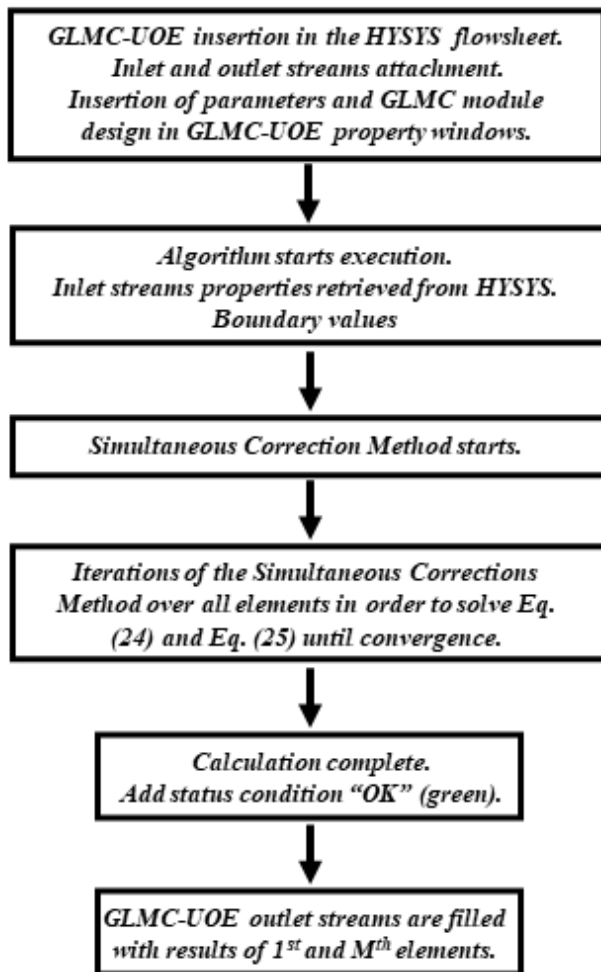
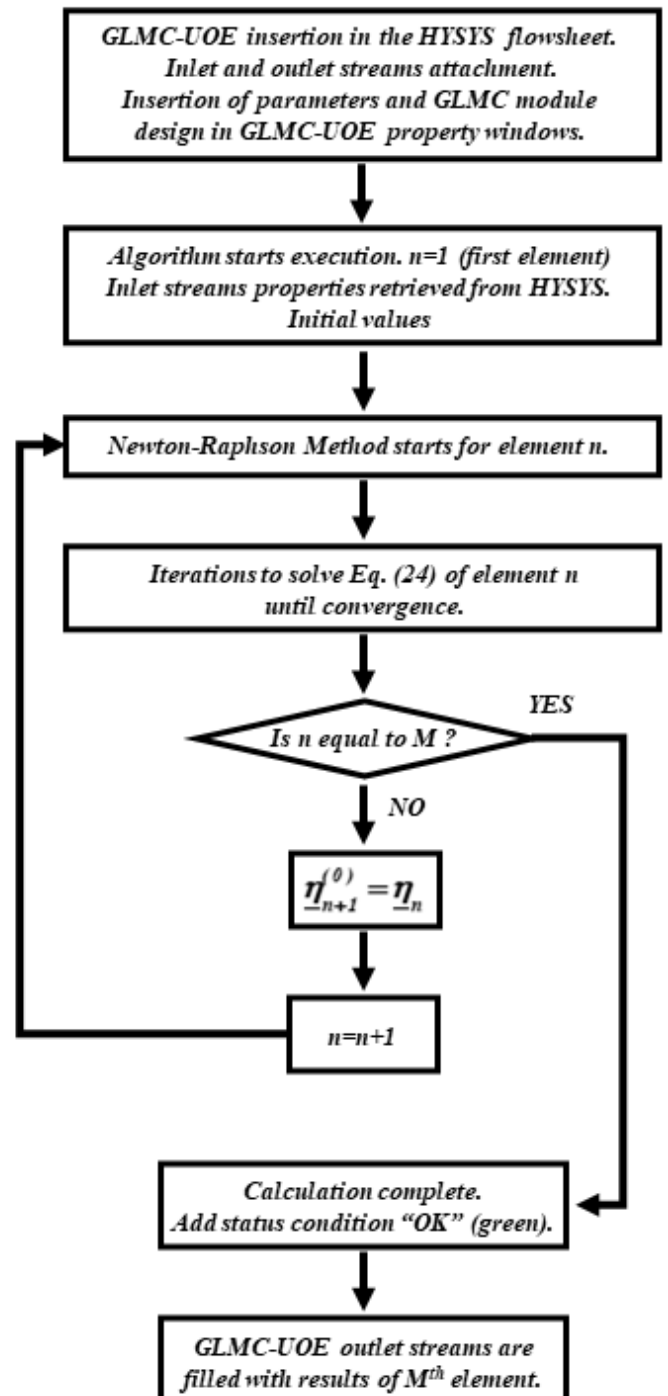
(a) GLMC-CCC-D Algorithm**(b) GLMC-PC-D Algorithm**

Figure 3. Algorithm flowcharts for solving: (a) a countercurrent-contact GLMC (GLMC-CCC-D) and (b) parallel-contact GLMC (GLMC-PC-D).

2.1.6. GLMC-UOE Validation

Appendices A–D report GLMC-UOE validation against the literature data. Appendix A validates GLMC-PC-D via the reproduction of the results of de Medeiros et al. [54] for NG decarbonation with aqueous-MEA-MDEA through a parallel-contact GLMC. Appendix B asymptotically validates an adiabatic GLMC-PC-D for NG decarbonation with aqueous-MEA-MDEA against HYSYS P-H flash. The principle here is that a parallel-contact GLMC-PC-D with a large transfer area asymptotically approaches the response of an adiabatic

pressure–enthalpy (P-H) flash with the same parallel feeds. Appendix C asymptotically validates the adiabatic GLMC-CCC-D for NG decarbonation with aqueous-MEA-MDEA against an HYSYS absorption column, because an adiabatic countercurrent-contact GLMC-CCC-D with a large transfer area asymptotically approaches the response of a large adiabatic absorption column with the same countercurrent feed. Appendix D validates the adiabatic GLMC-CCC-D model via the reproduction of the adiabatic countercurrent GLMC results of Belaissaoui and Favre [47] for biogas decarbonation with pressurized water.

In this work, the proposed landfill-gas-to-biomethane route adopts the GLMC modules of Belaissaoui and Favre [47] with a pressurized-water solvent for landfill-gas decarbonation/desulfurization, i.e., the same modules, solvent ($T = 15\text{ }^{\circ}\text{C}$, $P = 7\text{ bar}$), and $\text{H}_2\text{O}/\text{CO}_2$ capture-ratio were used. The used GLMC mass transfer coefficients were those obtained from Appendix D for GLMC-CCC-D validation. Since Belaissaoui and Favre [47] adopt isothermal GLMC modeling—which precludes obtaining the GLMC internal heat transfer coefficient, U_I , for landfill-gas decarbonation/desulfurization with pressurized water— U_I was estimated using an ad hoc asymptotic procedure in Appendix E.

2.2. Landfill-Gas Composition

Landfill-gas $\text{CH}_4/\text{CO}_2/\text{H}_2\text{S}/\text{H}_2\text{O}$ compositions (Table 2) were obtained from Länstelä et al. [76]. Regarding the siloxanes (Table 1), the predominant species in landfill-gas are usually D4/D5 [84], and the lack of L3/L5/TMS compositions is not uncommon [20]. Thus, the present work contemplates seven siloxanes: L2/L4/L6/D3/D4/D5/D6 (all in the HYSYS Library). The landfill-gas from landfill LF-1 [20] was used for defining L2/L4/L6/D3/D4/D5/D6 contents (Table 1).

Table 2. Landfill-gas decarbonation/desulfurization siloxane-removal simulation/design assumptions.

Topic	Description
Thermodynamic Modeling	Landfill-Gas Compression, $\text{CO}_2/\text{H}_2\text{S}$ Separation, Siloxanes Separation: HYSYS Acid-Gas Physical-Solvents Package; CO_2 -to-EOR: PR-EOS; Cooling-Water(CW)/Chilled-Water(ChW)/LPS,MPS: HYSYS ASME-Steam-Table;
Landfill-Gas	$0.5\text{ MMNm}^3/\text{d}$; $T = 30\text{ }^{\circ}\text{C}$; $P = 1\text{ bar}$; $\text{Mol} = 27.73\text{ g/mol}$; $\text{CH}_4 = 55.7\text{ \%mol}$; $\text{CO}_2 = 40\text{ \%mol}$; $\text{H}_2\text{O}^{\text{Saturation}} = 4.28\text{ \%mol}$; $\text{H}_2\text{S} = 150\text{ ppm-mol}$; Siloxanes: Table 1.
Biomethane	$\text{CH}_4 \geq 85\text{ \%mol}$; $\text{CO}_2 \leq 3\text{ \%mol}$; $\text{H}_2\text{S} \leq 10\text{ mg/Nm}^3$; Siloxanes $\leq 0.03\text{ mg/Nm}^3$ [19,85,86]
GLMC Module [47]	HFM: Polyphenylene-Oxide (Parker P-240); $d_i = 370\text{ }\mu\text{m}$; $d_o = 520\text{ }\mu\text{m}$; HFM-Side:Landfill-Gas; Shell-Side:Water; $D = 0.36\text{ m}$; Packing-Ratio: $\phi = 0.5$; $N_{\text{HF}} = 2.39 \times 10^5\text{ fibers}$; GLMC-Absorber: $A_{\text{GLMC}} = 663.65\text{ m}^2/\text{module}$; $Z_M = 2\text{ m}$; GLMC-Stripper: $A_{\text{GLMC}} = 1991.85\text{ m}^2/\text{module}$; $Z_M = 6\text{ m}$;
GLMC Modeling	$U_I^{\text{GLMC-CCC-D}} = U_I^{\text{GLMC-PC-D}} = 0.09\text{ Wm}^{-2}\text{K}^{-1}$; $U_E = 0$; $\Pi_{\text{CO}_2} = \Pi_{\text{H}_2\text{S}} = \Pi_{\text{H}_2\text{O}} = 6.5756 \times 10^{-4}\text{ mol}/(\text{s.bar.m}^2)$; $\Pi_{\text{CH}_4} = 3.868 \times 10^{-5}\text{ mol}/(\text{s.bar.m}^2)$; $\Pi_{\text{Siloxanes}} = 0$; Capture-Ratio = $443.41\text{ kg}^{\text{H}_2\text{O}}/\text{kg}^{\text{CO}_2}$; {TS} = { CO_2 , H_2S , CH_4 , H_2O }; GLMC-CCC-D: Countercurrent-Contact Distributed-Model (Section 2.1); GLMC-PC-D: Parallel-Contact Distributed-Model (Section 2.1).
High-Pressure $\text{CO}_2/\text{H}_2\text{S}$ Reboilerd Stripper	Feed[$\text{H}_2\text{O}/\text{CO}_2/\text{H}_2\text{S}$] = $7,275,950\text{ kg/h}$; $P^{\text{Feed}} = 30.14\text{ bar}$; $T^{\text{Feed}} = 223.2\text{ }^{\circ}\text{C}$; Stages ^{Theoretical} = 10; Feed-Stage = 5; $P^{\text{Condenser}} = 30\text{ bar}$; $T^{\text{Condenser}} = 40\text{ }^{\circ}\text{C}$; $P^{\text{Reboiler}} = 30.2\text{ bar}$; $T^{\text{Reboiler}} = 233.8\text{ }^{\circ}\text{C}$; Condenser: Total-Reflux; Reboiler: Kettle (MPS); Reflux-Ratio ^{Top} = 721.6.
DEPG Absorber	Solvent: 35.06 kmol/h ; DEPG = 98.4 \%w/w ; $\text{H}_2\text{O} = 1.6\text{ \%w/w}$; $P = 6.9\text{ bar}$; $T = 15\text{ }^{\circ}\text{C}$; $P_V^{\text{in}} = 6.995\text{ bar}$; $T_V^{\text{in}} = 17.29\text{ }^{\circ}\text{C}$; Stages ^{Theoretical} = 20.
DEPG Reboilerd Stripper	Feed: 36.85 kmol/h ; $P^{\text{Feed}} = 1.17\text{ bar}$; $T^{\text{Feed}} = 162.7\text{ }^{\circ}\text{C}$; Stages ^{Theoretical} = 10; Feed-Stage = 5; $P^{\text{Condenser}} = 1.1\text{ bar}$; $T^{\text{Condenser}} = 88.72\text{ }^{\circ}\text{C}$; $P^{\text{Reboiler}} = 1.2\text{ bar}$; $T^{\text{Reboiler}} = 175\text{ }^{\circ}\text{C}$; Condenser: Total-Reflux; Reboiler: Kettle (LPS); Reflux-Ratio ^{Top} = 100.

Table 2. Cont.

Topic	Description
Saturated-Steam [87]	Low-Pressure-Steam (LPS): $P = 14.3$ bar, $T = 196$ °C; Medium-Pressure-Steam (MPS): $P = 42.5$ bar, $T = 254$ °C.
Compressors	Adiabatic-Efficiency = 75%; Compression-Ratio ^{Stage} = 3 (Landfill-Gas); Compression-Ratio ^{Stage} = 2.25 (CO ₂ -to-EOR).
Pumps	Adiabatic-Efficiency = 75%.
Intercoolers	$T^{\text{Gas-Out}} = 40$ °C; $\Delta P^{\text{Gas}} = 0.5$ bar.
Exchangers	$\Delta T^{\text{Approach}} = 10$ °C; $\Delta P = 0.5$ bar.
Cooling-Water	$T_{\text{CW}}^{\text{in}} = 30$ °C; $T_{\text{CW}}^{\text{out}} = 45$ °C; $P_{\text{CW}}^{\text{in}} = 4$ bar; $P_{\text{CW}}^{\text{out}} = 3.5$ bar.
Chilled-Water	$T_{\text{ChW}}^{\text{in}} = 10$ °C; $T_{\text{ChW}}^{\text{out}} = 15$ °C; $P_{\text{ChW}}^{\text{in}} = 4$ bar; $P_{\text{ChW}}^{\text{out}} = 3.5$ bar.

2.3. Landfill-Gas-to-Biomethane Simulation Assumptions

Table 2 shows the simulation assumptions for the proposed landfill-gas-to-biomethane process.

2.4. Landfill-Gas-to-Biomethane Process

The proposed GLMC-based industrial-scale landfill-gas-to-biomethane process is described in this section. Figure 4 shows a block diagram with the interconnection between the process units, which are detailed in the following subsections.

2.4.1. Landfill-Gas Pre-Processing and Compression

Landfill-gas is collected via sufficiently deep landfill wells avoiding air penetration [1], such that O₂/N₂ contents are negligible. Landfill-gas pre-purification removes solid/liquid particulates.

Water-saturated landfill-gas in atmospheric conditions is compressed to $P = 7$ bar via 2-staged intercooled compression (Figure 5). In each compression stage, the temperature should not surpass 150 °C, otherwise compressors can be damaged. Intercoolers cool down the gas to 40 °C with cooling-water (CW), whose operating conditions are defined in Table 2. Knock-out vessel aqueous condensates are collected for further treatment (out of scope). Compressed landfill-gas feeds the GLMC battery for decarbonization/desulfurization.

2.4.2. Intensified GLMC Decarbonation/Desulfurization with Pressurized Water

CO₂/H₂S removal from landfill-gas was performed (Figure 6) in an intensified GLMC battery with $N_M = 333$ modules in countercurrent contact with pressurized water ($P = 7$ bar, $T = 15$ °C). The pressure should be higher than atmospheric pressure to increase CO₂/H₂S fugacities in the landfill-gas, improving the mass transfer driving force. The low solvent temperature (15 °C) improves CO₂/H₂S solubility [47]. The decarbonized/desulfurized landfill-gas was subjected to siloxane removal, while rich-water was pumped to another intensified operation, namely, a high-pressure CO₂ stripper. The rich-water was firstly pre-heated with hot, lean-water from the stripper reboiler in a thermal-integration water–water heat exchangers, where $\Delta T^{\text{Approach}} = 10$ °C. Unlike ethanolamines, water is insensitive to high temperatures, allowing water regeneration via high pressure ($P = 30$ bar) CO₂/H₂S stripping. This drastically reduces CO₂ compression costs, but operations above 30 bar are not advisable as column construction costs would be prohibitively higher [82]. The reboiler operated at 233.8 °C and was heated by saturated medium-pressure steam (MPS). The stripper top gas was water-saturated CO₂ with some H₂S ($P = 30$ bar) at a total reflux condenser temperature of 40 °C. The lean-water returned to the GLMC battery after cooling with chilled-water (ChW) to $T = 15$ °C. Chilled-water was produced via a propane refrigeration cycle, whose simulation is not in the scope of the present study. Some excess water (from landfill-gas) was collected, i.e., water make-up was unnecessary.

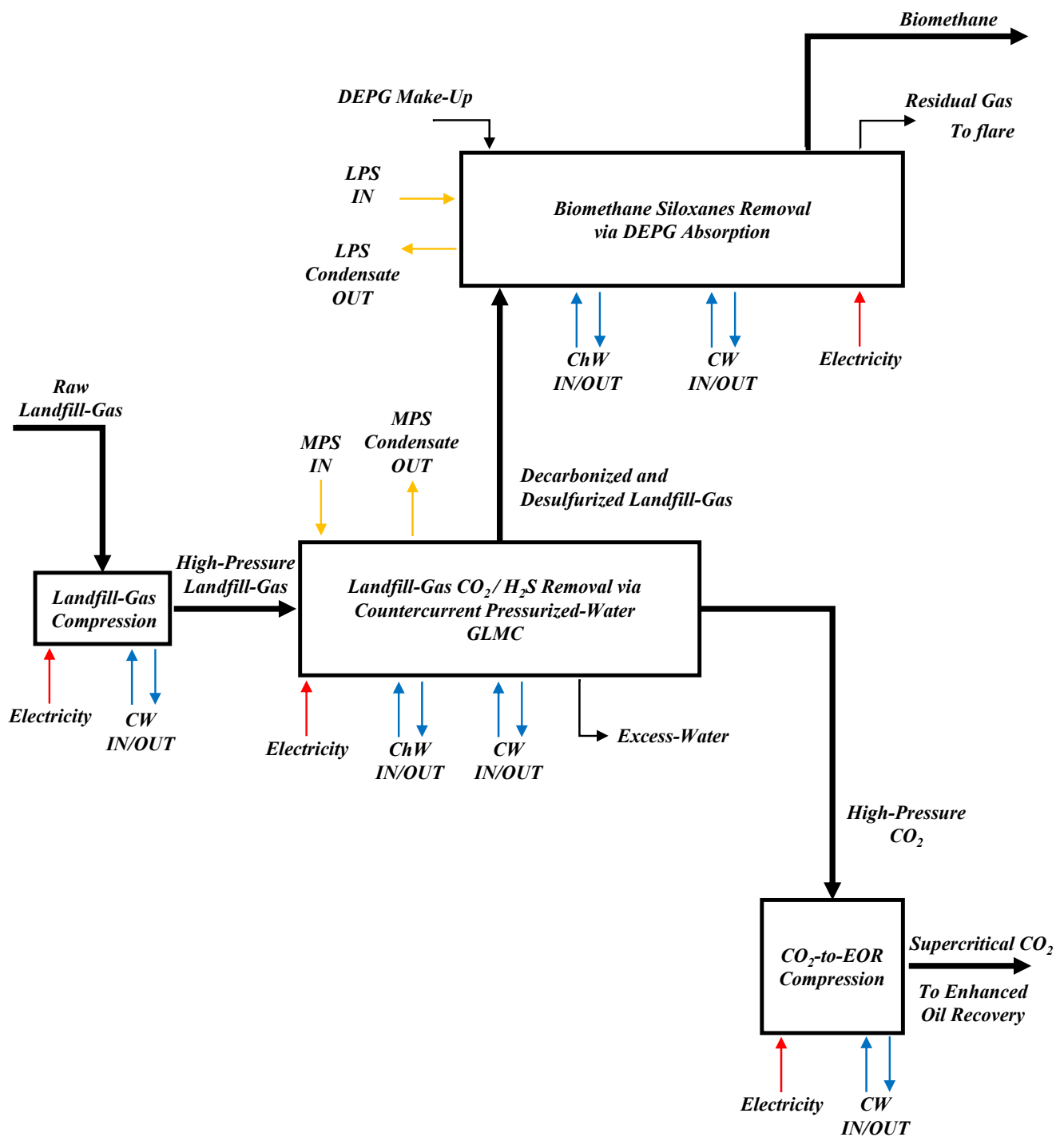


Figure 4. Block diagram of GLMC-based industrial-scale landfill-gas-to-biomethane process.

Water-saturated CO₂ from the stripper was compressed from $P = 30$ bar to $P = 150.3$ bar via 2-staged intercooled compression (Figure 7). Curiously, knock-out vessels were not necessary, since water vapor is stabilized by high-pressure CO₂ at $T = 40$ °C after cooling with CW. At $P = 150.3$ bar ($T = 40$ °C), CO₂ becomes supercritical, requiring the pump to reach $P = 300$ bar for EOR exportation.

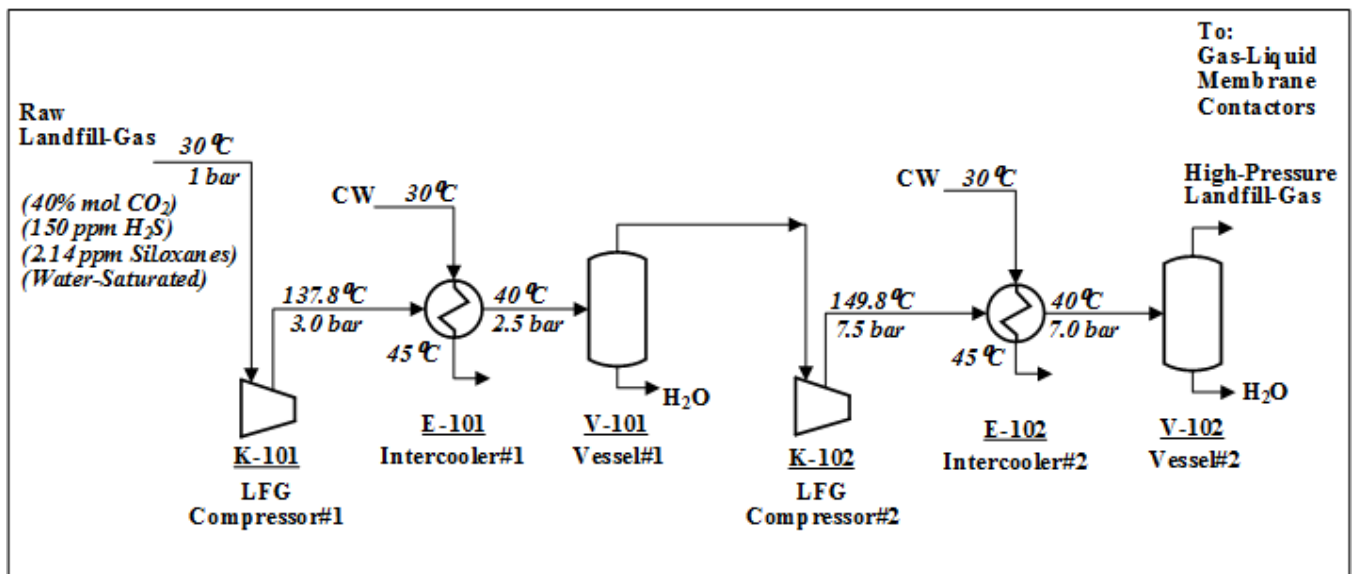


Figure 5. Landfill-gas compression.

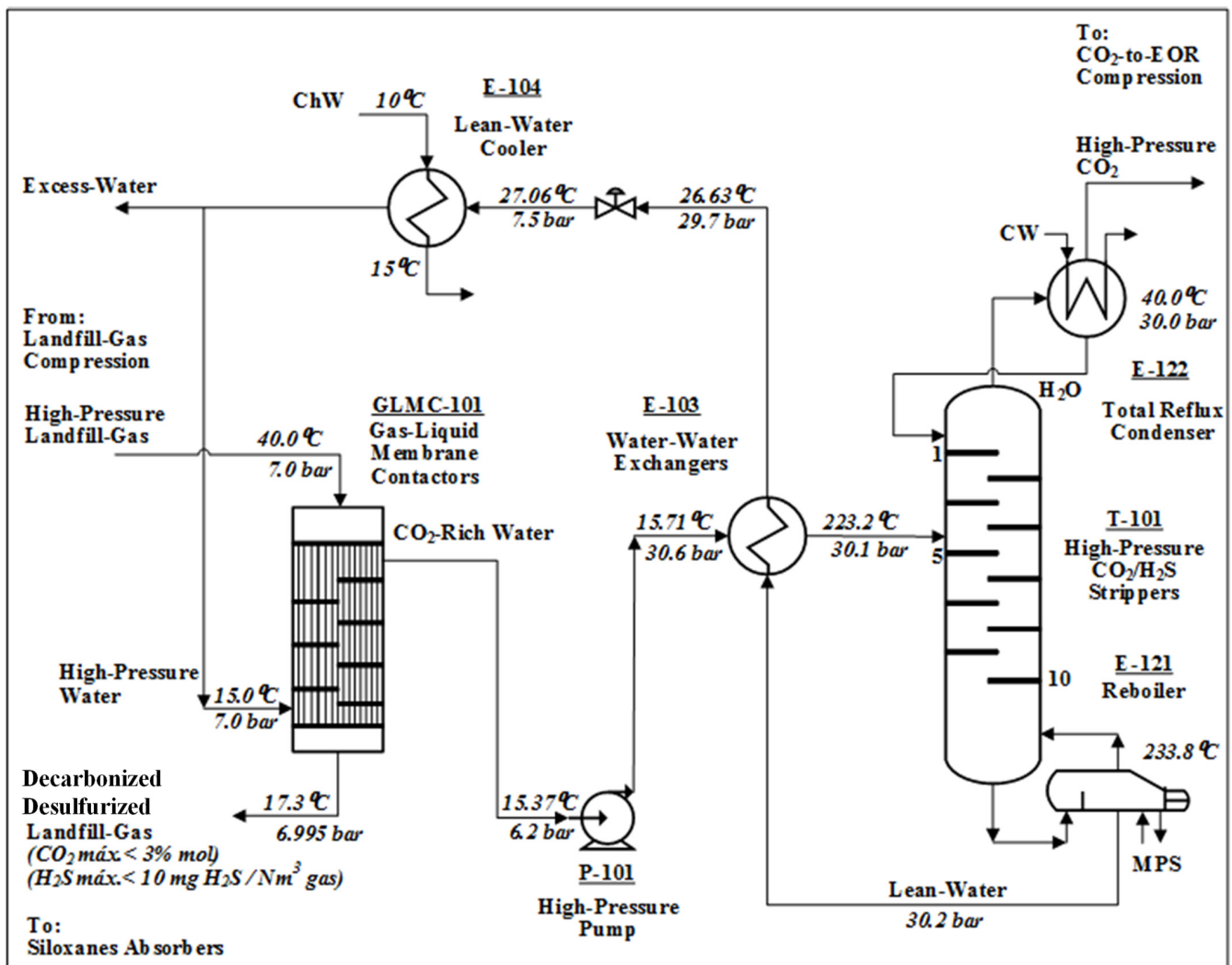


Figure 6. Landfill-gas CO₂/H₂S removal via countercurrent pressurized-water GLMC.

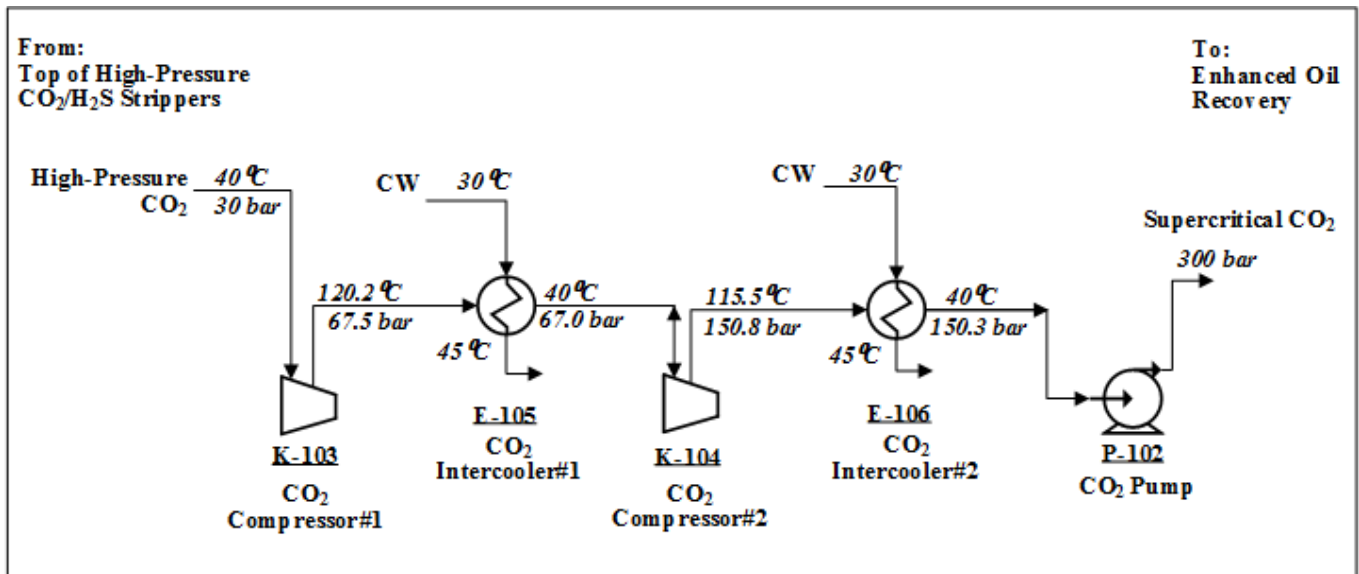


Figure 7. CO₂-to-EOR compression.

2.4.3. Siloxane Removal via DEPG Absorption

Decarbonated/desulfurized landfill-gas from the GLMC passes through DEPG absorption for siloxane removal at $P = 7$ bar and $T = 15$ °C (Figure 8). The low temperature favors siloxanes solubility in DEPG. Landfill-gas feeds through the absorber bottom while lean-DEPG is fed at the top. The top gas is biomethane with less than $0.03 \text{ mg}^{\text{Siloxanes}}/\text{Nm}^3$, the limit of capstone microturbines [19]. Rich DEPG passes through heat exchangers for preheating with hot lean DEPG from the DEPG stripper reboiler ($\Delta T^{\text{Approach}} = 10$ °C). Rich-DEPG depressurizes to $P = 1.17$ bar to feed the atmospheric DEPG stripper, whose reboiler operates at $T \leq 175$ °C to avoid DEPG thermal decomposition [17]. The total reflux condenser operates at $T = 88.7$ °C to favor the release of siloxanes in the top gas, which also contains CO₂/H₂O/H₂S/CH₄. This stream is cooled down to $T = 40$ °C, condensing some water in a knock-out vessel. The final residual-gas is flared to avoid CH₄ and siloxane emissions. Lean-DEPG is pumped and cooled down to $T = 15$ °C with chilled-water before returning to the absorber. DEPG make-up is negligible.

compressed landfill-gas ($P = 7$ bar, $T = 40$ °C). Table 3 presents V/L inlet/outlet component fugacities for GLMC-CCC-D and GLMC-PC-D, while Table 4 shows inlet/outlet streams and $\text{CO}_2/\text{H}_2\text{S}$ %Recoveries evincing that, with the same transfer area and capture-ratio, only the GLMC-CCC-D battery can achieve $\text{CH}_4/\text{CO}_2/\text{H}_2\text{S}$ biomethane specifications (Table 2). The reason is the higher fugacity-difference driving force in the countercurrent GLMC-CCC-D. This is the reason for using a GLMC-CCC-D battery (Section 2.4) in the landfill-gas-to-biomethane intensified process. The results of the GLMC-PC-D are depicted via the following axial profiles in Figure 9: $\hat{f}_{\text{CO}_2}^V, \hat{f}_{\text{CO}_2}^L, \hat{f}_{\text{CH}_4}^V, \hat{f}_{\text{CH}_4}^L$ (Figure 9a); V %mol CO_2/CH_4 (Figure 9b); $\hat{f}_{\text{H}_2\text{S}}^V, \hat{f}_{\text{H}_2\text{S}}^L$ (Figure 9c); V ppm-mol H_2S (Figure 9d); $\hat{f}_{\text{H}_2\text{O}}^V, \hat{f}_{\text{H}_2\text{O}}^L$ (Figure 9e); V %mol H_2O (Figure 9f); $\text{H}_2\text{S}/\text{CO}_2$ %Recovery and CH_4 %Loss (Figure 9g); and CO_2/CH_4 Selectivity (Figure 9h). It is interesting to see (Table 3) that, for $\text{CO}_2/\text{H}_2\text{S}/\text{CH}_4$ species, $\hat{f}_k^V > \hat{f}_k^L$ throughout the GLMC-PC-D process due to parallel $V \rightarrow L$ transfer, while $\hat{f}_k^{V\text{OUT}} > \hat{f}_k^{L\text{IN}}, \hat{f}_k^{V\text{IN}} > \hat{f}_k^{L\text{OUT}}$ in the GLMC-CCC-D process due to countercurrent $V \rightarrow L$ transfer.

Table 3. Inlet/outlet fugacities: GLMC-CCC-D ($M = 5$) and GLMC-PC-D ($M = 100$).

Streams	Fugacity	CO_2	CH_4	H_2S	H_2O
Inlets	\hat{f}_k^V (bar)	2.812	3.989	1.048×10^{-3}	0.074
	\hat{f}_k^L (bar)	1.602×10^{-9}	0	0	0.017
GLMC-CCC-D Outlets	\hat{f}_k^V (bar)	0.203	6.669	3.318×10^{-5}	0.019
	\hat{f}_k^L (bar)	1.190	3.899	1.505×10^{-4}	0.018
GLMC-PC-D Outlets	\hat{f}_k^V (bar)	0.989	5.876	1.448×10^{-4}	0.018
	\hat{f}_k^L (bar)	0.977	5.120	1.403×10^{-4}	0.017

Table 4. Landfill-gas decarbonation/desulfurization results: GLMC-CCC-D and GLMC-PC-D batteries.

	Landfill-Gas Inlet	Water Inlet	GLMC-CCC-D Landfill-Gas Outlet	GLMC-CCC-D Water Outlet	GLMC-PC-D Landfill-Gas Outlet	GLMC-PC-D Water Outlet
P (bar)	7.0	7.0	6.995	6.213	6.996	6.211
T (°C)	40.00	15.00	17.29	15.37	21.11	15.32
MMNm ³ /d	0.483961	-	0.261854	-	0.286783	-
kg/h	-	7,259,307	-	7,275,950	-	7,273,439
H_2O (%mol)	1.11 *	100	0.29	99.90	0.28	99.91
CH_4 (%mol)	57.55	2.06×10^{-23}	96.71	0.01	85.14	0.02
CO_2 (%mol)	41.32	1.20×10^{-10}	3.0	0.09	14.59	0.07
H_2S (ppm-mol)	154.94	2.77×10^{-13}	4.94	0.34	21.53	0.32
D3 (ppb-mol) #	50.97	0	94.21	0	86.02	0
D4 (ppb-mol) #	977.59	0	1806.79	0	1649.73	0
D5 (ppb-mol) #	1.16	0	2.15	0	1.96	0
D6 (ppb-mol) #	12.46	0	23.03	0	21.03	0
L2 (ppb-mol) #	865.09	0	1598.87	0	1459.89	0
L4 (ppb-mol) #	2.84	0	5.24	0	4.79	0
L6 (ppb-mol) #	0.50	0	0.93	0	0.85	0
Siloxanes (ppb-mol) #	1910.61	0	3531.22	0	3224.27	0
Final Results: Gas-to-Solvent $\text{CO}_2/\text{H}_2\text{S}$ %Recoveries and Gas-to-Solvent CH_4 %Loss						
GLMC Battery	%Recovery CO_2		%Recovery H_2S		%Loss CH_4	
GLMC-PC-D	79.08		91.77		12.33	
GLMC-CCC-D	96.08		98.28		9.07	

* Water saturated; # Siloxanes: non-transferable.

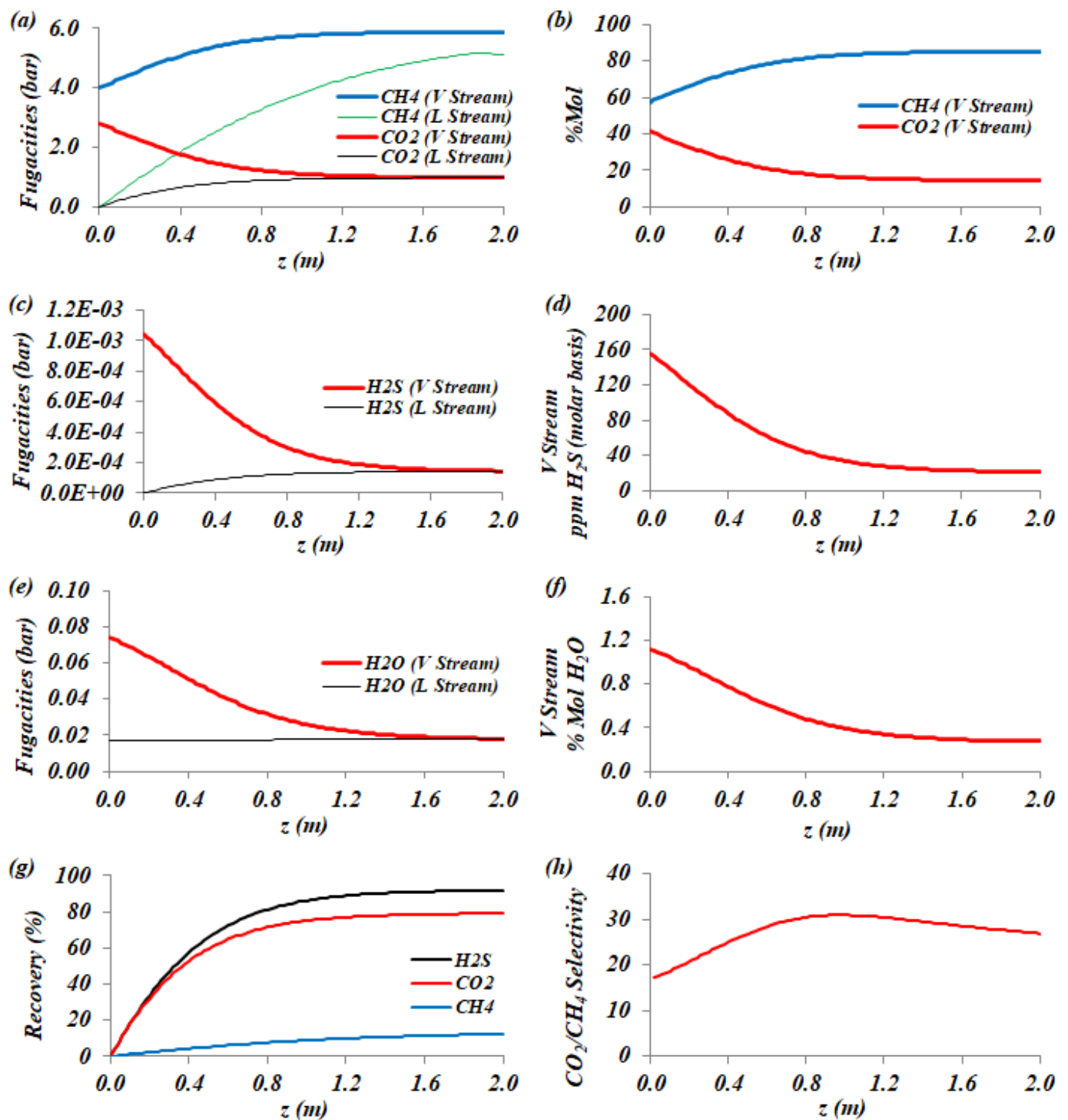


Figure 9. GLMC-PC-D axial profiles: (a) $f_{CO_2}^V, f_{CO_2}^L, f_{CH_4}^V, f_{CH_4}^L$; (b) V (%mol) CO_2/H_2S ; (c) $f_{H_2S}^V, f_{H_2S}^L$; (d) V ppm-mol H_2S ; (e) $f_{H_2O}^V, f_{H_2O}^L$; (f) V (%mol) H_2O ; (g) %Recovery, % CH_4 Loss; (h) CO_2/CH_4 Selectivity.

GLMC-PC-D fugacity profiles evince the inefficiency of parallel contact, as transfer driving forces start high and then vanish rapidly, limiting CO_2/H_2S transfer, as seen in Table 3 and Figure 9a–c. In the study of Zhang et al. [39], which tested the increase in the solvent flowrate to decrease CO_2 fugacity in the aqueous phase, it was also observed that it contributes to achieving extra CO_2 mass transfer driving force. On the other hand, in the

GLMC-CCC-D process, a higher driving force is maintained because, as V approaches the outlet, it contacts decreasing \hat{f}_k^L values. Moreover, in the GLMC-PC-D process, Figure 9a shows that CO_2 transfer slows down at $z = 1.4$ m, suggesting that the battery is oversized for CO_2 transfer via parallel contact, benefiting parasitic CH_4 $V \rightarrow L$ transfers. Meanwhile, at $z = 1.95$ m, L becomes a two-phase component due to $V \rightarrow L$ CH_4 transfer, and $\hat{f}_{\text{CH}_4}^L$ starts decreasing with a tendency to maintain the CH_4 driving force. This effect creates CH_4 bubbles in the L stream generating $\text{CO}_2/\text{H}_2\text{S}$ stripping from the solvent that lowers $\hat{f}_{\text{CH}_4}^L$. This behavior of CO_2 and CH_4 driving forces decreases CO_2/CH_4 selectivity (Figure 9h) in the 2nd half of Z_M . All these aspects of the GLMC-PC-D process were similarly observed by de Medeiros et al. [54]. Figure 9e,f depict strong $V \rightarrow L$ water transfer driven by the lower L temperature ($\hat{f}_{\text{H}_2\text{O}}^L < \hat{f}_{\text{H}_2\text{O}}^V$). This makes landfill-gas decarbonation/desulfurization self-sufficient in water (i.e., water make-up is unnecessary and the process exports water). This behavior is in accordance with Ghasem et al.'s study [53], which previously demonstrated $L \rightarrow V$ water transfer, and also with Villeneuve et al.'s study [68], which showed bidirectional water transfer, i.e., $V \rightarrow L$ water transfer is also possible. The higher H_2S %Recovery rate comparative to its CO_2 counterpart (Figure 9g) results from a much higher H_2S capture ratio ($k_g^{\text{H}_2\text{O}}/k_g^{\text{H}_2\text{S}}$). Table 4 also shows inferior $\text{CO}_2/\text{H}_2\text{S}$ %Recoveries and a greater CH_4 %Loss of GLMC-PC-D compared to GLMC-CCC-D, the former due to poor driving-force utilization and the latter due to the oversized battery for parallel contact benefiting CH_4 $V \rightarrow L$ transfer.

Figure 10 presents the GLMC-PC-D temperature/pressure profiles. Regarding the thermal effects, a paramount factor is the high solvent/gas mass ratio (besides $\bar{C}_P^L \approx 2\bar{C}_P^V$) to provide a high CO_2 capture ratio ($443.41 \text{ kg}^{\text{H}_2\text{O}}/\text{kg}^{\text{CO}_2}$). As a consequence, T_L slightly increases while T_V quenches rapidly toward T_L (Figure 10a), mainly due to $V \rightarrow L$ heat transfer and the $V \cdot \bar{C}_P^V$ reduction due to CO_2 $V \rightarrow L$ transfer. Evidently, part of the small T_L value increase comes from exothermic physical absorption. The high solvent/gas mass ratio entails a high shell-side L pressure drop compared to the low HFM-side V pressure drop (Figure 10b). These aspects are clear advantages in comparison with the incomplete isothermal/isobaric GLMC model of Belaissaoui and Favre [47].

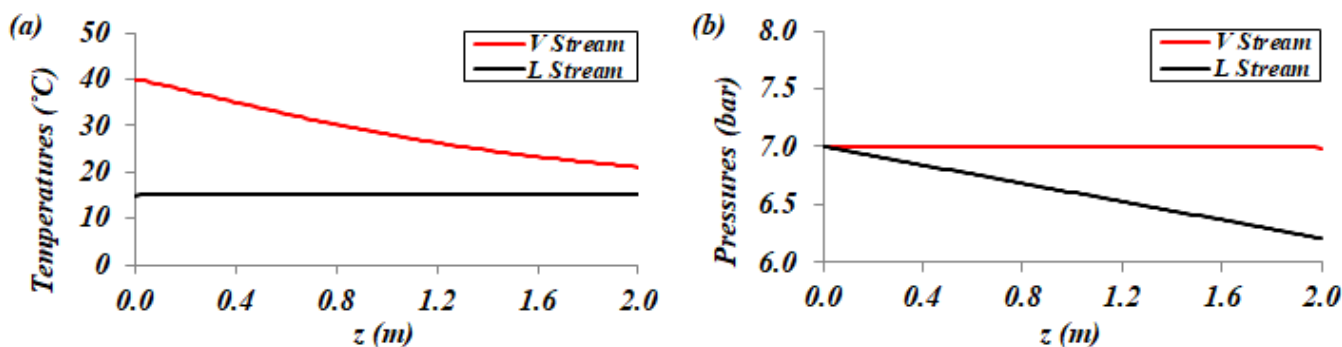


Figure 10. GLMC-PC-D axial profiles: (a) temperatures; (b) pressures.

GLMC-CCC-D's and GLMC-PC-D's performance comparison leads to the selection of the GLMC-CCC-D battery in the landfill-gas-to-biomethane process. Thus, the rich water from GLMC-CCC-D is regenerated via high-pressure ($P = 30$ bar) stripping (Figure 6). Table 5 shows the landfill-gas decarbonation/desulfurization balance and the high-pressure stripper outlets. The stripper regenerates water while releasing CO_2 at $P = 30$ bar, thus lowering CO_2 -to-EOR compression investment and power. Some authors naively suggest low-pressure CO_2 stripping for GLMCs with water [89], evidently entailing much higher compression power for CO_2 utilization.

Table 5. Landfill-gas decarbonation/desulfurization balance and high-pressure stripper products.

	Inlet Landfill-Gas	Outlet Landfill-Gas	Stripper Top Gas	Excess Water
H ₂ O (kmol/h)	10.03	1.43	1.28	7.32
CH ₄ (kmol/h)	518.05	471.05	47.00	1.94×10^{-24}
CO ₂ (kmol/h)	372.00	14.59	357.41	1.11×10^{-11}
H ₂ S (kmol/h)	0.1395	0.0024	0.1371	5.41×10^{-18}
High-Pressure CO ₂ /H ₂ S Stripper—Water Regeneration				
		Stripper Top Gas	Lean Water	
P (bar)		30.0	30.2	
T (°C)		40.0	233.8	
kmol/h		405.82	402,960.11	
MMNm ³ /d		0.218	-	
H ₂ O (%mol)		0.31	100	
CH ₄ (%mol)		11.58	2.65×10^{-23}	
CO ₂ (%mol)		88.07	1.52×10^{-10}	
H ₂ S (ppm-mol)		337.78	7.39×10^{-13}	

3.2. Siloxane Separation, Process Waste, and Power/Utilities Consumption

GLMC-CCC-D outlet landfill-gas experiences siloxane separation via DEPG absorption (Figure 8), as suggested by Ajhar et al. [75]. Table 6 shows the outlets of the DEPG absorber and DEPG stripper, confirming that biomethane CH₄/CO₂/H₂S/Siloxane specifications were attained. But, biomethane still has 3100 ppm-mol H₂O requiring further dehydration. Table 7 depicts siloxane separation balance, waste streams with high siloxane/H₂S contents (demanding disposal), and process power/utilities consumption values.

Table 6. Siloxane DEPG absorber and DEPG stripper.

	Biomethane Outlet	Absorber Rich DEPG	Stripper Top Gas	Lean DEPG
P (bar)	6.9	6.995	1.1	1.2
T (°C)	15.84	19.35	88.72	175
kmol/h	485.28 (0.26 MMNm ³ /d)	36.86	1.80	35.06
DEPG (%mol)	3.72×10^{-6}	75.98	1.74×10^{-18}	79.87
H ₂ O (%mol)	0.31	22.12	61.09	20.13
CH ₄ (%mol)	96.97	1.24	25.54	2.65×10^{-25}
CO ₂ (%mol)	2.96	0.65	13.26	7.95×10^{-15}
H ₂ S (ppm-mol)	4.36 (6.7 mg/Nm ³)	7.77	159.44	5.33×10^{-14}
D3 (ppm-mol)	1×10^{-19}	1.25	25.6	3×10^{-17}
D4 (ppm-mol)	6×10^{-18}	23.9	490	8×10^{-15}
D5 (ppm-mol)	0.00145	12.2	8×10^{-7}	12.8
D6 (ppm-mol)	0.00025	57.2	5.09	59.9
L2 (ppm-mol)	2×10^{-9}	21.1	434	9×10^{-19}
L4 (ppm-mol)	0.00001	0.1935	1.59	0.122
L6 (ppm-mol)	4×10^{-23}	0.0123	0.253	1.5×10^{-17}
Siloxanes (ppm-mol)	0.0017 (0.029 mg/Nm ³)	116	957	72.8

Table 7. Siloxane separation balance, waste streams, and power/utilities consumption.

	Inlet Landfill-Gas	Outlet Biomethane	Top-Gas Stripper	DEPG Make-Up
DEPG (kmol/h)	0	1.81×10^{-5}	3.13×10^{-20}	1.81×10^{-5}
H ₂ O (kmol/h)	1.43	0.33	1.10	0
CH ₄ (kmol/h)	471.05	470.59	0.46	-
CO ₂ (kmol/h)	14.59	14.35	0.24	-
H ₂ S (kmol/h)	0.0024	0.0021	0.0003	-
Siloxanes (kmol/h)	1.72×10^{-3}	8.28×10^{-7}	1.72×10^{-3}	-
	Process Wastes		Power and Utilities Consumption	
	Residual Gas	Residual Water	Consumption	
kmol/h	0.76	1.04	Power	9.41 MW
DEPG (%mol)	0	0	Chilled Water	16,461 t/h
H ₂ O (%mol)	7.44	99.99	Cooling Water	225,507 t/h
CH ₄ (%mol)	60.77	0.00124	LPS	4 t/h
CO ₂ (%mol)	31.53	0.01	MPS	8604 t/h
H ₂ S (ppm-mol)	378.76	0.45		
Siloxanes (ppm-mol)	2200	7.71		

4. Conclusions

A novel GLMC-intensified landfill-gas-to-biomethane process was disclosed, where the decarbonation/desulfurization of 0.5 MMNm³/d of landfill-gas were conducted in a battery of countercurrent GLMC modules using a pressurized-water solvent ($P = 7$ bar, $T = 15$ °C). Since water absorption is inefficient for siloxane removal, siloxanes were removed after decarbonation/desulfurization via DEPG absorption ($P = 6.9$ bar, $T = 15$ °C) with a small DEPG circulation rate, where DEPG regeneration was conducted via atmospheric stripping requiring a negligible DEPG make-up. A GLMC water solvent is regenerated via intensified high-pressure CO₂ stripping, lowering CO₂-to-EOR compression costs. This process dismisses water make-up and exports water. There are only two small waste streams with high siloxane/H₂S contents. The main revenues comprise clean 0.26 MMNm³/d biomethane and 0.218 MMNm³/d of dense CO₂ traded as an EOR agent. Power consumption reaches 9.41 MW, including CO₂-to-EOR compression/pumping. To the authors' knowledge, quantitative multicomponent siloxane removal from decarbonated/desulfurized landfill-gas has never been attempted in the literature. The landfill-gas-to-biomethane process proved to be technically viable, attaining CH₄ (>85%mol), CO₂ (<3%mol), H₂S (<10 mg/Nm³), and siloxane (<0.03 mg/Nm³) specifications. Even if biomethane is burned without CCS, due to CO₂ capture from landfill-gas and EOR utilization, the present landfill-gas-to-biomethane results represent BECCS implementation.

To simulate GLMC landfill-gas decarbonation/desulfurization, a thermodynamically rigorous 1D GLMC steady-state model—GLMC-UOE—was developed. GLMC-UOE runs, integrated into Aspen-HYSYS 10.0, as a new HYSYS unit operation using the HYSYS Acid-Gas Physical-Solvents Thermodynamic Package (as well as the HYSYS Chemical Solvents Package). GLMC-UOE can simulate countercurrent-contact 1D-distributed GLMCs with the GLMC-CCC-D model and parallel-contact 1D-distributed GLMCs with the GLMC-PC-D model. Both models were validated via literature comparisons and can handle multicomponent bidirectional transmembrane heat/mass transfers, two-phase V/L flows, and rigorous V/L mass/energy/momentum balances predicting composition/temperature/pressure changes.

After the calibration of component permeances with the literature data, GLMC-UOE can perform rigorous steady-state simulations of landfill-gas decarbonation/desulfurization using a GLMC with pressurized water. This way, GLMC-UOE is useful to design new industrial-scale landfill-gas-to-biomethane projects to perform plant retrofitting, predict process changes

during scale-up/scale-down procedures, and to be used for process troubleshooting. The GLMC scale-up was demonstrated in Section 3.1 by using one of the main advantages of the GLMC concept: modularity. This way, the V flowrate can be increased/decreased, as long as the numbers of GLMC modules with the same design are added/removed proportionally in parallel, and the same hydrodynamic conditions for model validation are maintained, i.e., a constant V/L ratio and the same inlet temperatures/pressures.

It is worth noting that GLMC studies on landfill-gas commonly focus only on CO_2 removal, ignoring H_2S removal, water/ CH_4 bidirectional transmembrane transfers, temperature effects, and pressure drop, while, in this work, a GLMC was evaluated under multicomponent $\text{CO}_2/\text{CH}_4/\text{H}_2\text{S}/\text{H}_2\text{O}$ bidirectional transmembrane transfers with respective thermal effects and T/P changes. The GLMC-PC-D profiles proved that isothermal/isobaric GLMC modeling is inadequate, despite the GLMC literature's insistence of this assumption.

As a suggestion for future work, an economic analysis can be performed for novel landfill-gas-to-biomethane processes using GLMC decarbonation/desulfurization and siloxane removal via Selexol absorption.

Supplementary Materials: The following supporting information can be downloaded at: <https://www.mdpi.com/article/10.3390/pr12081667/s1>; Supplement S1 is in the Supplementary Materials, which can be found in the online version.

Author Contributions: Conceptualization, J.L.d.M. and O.d.Q.F.A.; data curation, G.P.d.C.; formal analysis, G.P.d.C. and J.L.d.M.; funding acquisition, J.L.d.M. and O.d.Q.F.A.; investigation, G.P.d.C. and J.L.d.M.; methodology, J.L.d.M. and O.d.Q.F.A.; project administration, J.L.d.M. and O.d.Q.F.A.; resources, J.L.d.M. and O.d.Q.F.A.; software, G.P.d.C.; supervision, J.L.d.M. and O.d.Q.F.A.; validation, G.P.d.C. and J.L.d.M.; visualization, G.P.d.C. and J.L.d.M.; writing—original draft, G.P.d.C. and J.L.d.M.; writing—review and editing, J.L.d.M. All authors have read and agreed to the published version of the manuscript.

Funding: JL de Medeiros and OQF Araújo acknowledge the financial support received from CNPq-Brazil (313861/2020-0, 312328/2021-4) and from FAPERJ Brazil (E-26/200.522/2023, E-26/201.178/2021).

Data Availability Statement: Data are contained within the article.

Conflicts of Interest: The authors declare no conflict of interest.

Abbreviations

1D: one-dimensional; BECCS: bioenergy with CCS; CCS: carbon capture and storage; ChW: chilled water; CW: cooling water; DEPG: Dimethyl-Ether Polyethylene-Glycol; EOR: enhanced oil recovery; GLMC: gas–liquid membrane contactor; GLMC-UOE: GLMC unit operation extension; GLMC-CCC-D countercurrent-contact GLMC distributed model; GLMC-PC-D: parallel-contact GLMC distributed model; HFM: hollow-fiber membrane; LPS: saturated low-pressure steam; MDEA: Methyl-diethanolamine; MEA: Monoethanolamine; MMNm^3/d : million normal m^3/d ; MPS: saturated medium-pressure steam; NG: natural gas; PR-EOS: Peng–Robinson equation of state; VLE: vapor–liquid equilibrium.

Nomenclature

A_{CSHF}, A_{CSS}	HFM-side and shell-side flow-section areas (m^2)
A_{GLMC}	GLMC module transfer area (m^2)
D, d_{HHF}, d_{HS}	Shell internal diameter, HFM-side hydraulic diameter, and shell-side hydraulic diameter (m)
d_i, d_o	Internal/external HFM diameters (m)
$\hat{f}_{k,n}^L, \hat{f}_{k,n}^V$	L/V species k fugacities at element n (bar)
$\Delta \hat{f}_{k,n}^{LM}$	Logarithmic mean of k transmembrane fugacity difference at element n (bar)
$\bar{H}_{k,n}^L, \bar{H}_{k,n}^V$	L/V k th partial molar enthalpies at element n (kJ/kmol)
$\bar{H}_{L,n}, \bar{H}_{V,n}$	L/V molar enthalpies at element n (kJ/kmol)
$h_{L,n}^S, h_{V,n}^{HF}$	Shell-side and HFM-side head losses for element n (Pa)
\underline{L}_n	Vector of species L molar flowrates leaving element n (mol/s)
M, N_{HF}	Number of discretized GLMC elements; number of HFMs per module

$N_{k,n}, N_M$	Transmembrane k transfer rate (mol/s) in element n and number of modules
p_{HF}	Center—center distance of adjacent HFMs (m)
P_{L_n}, P_{V_n}	L/V pressures of element n (bar)
ΔT_n^{LM}	Logarithmic mean transmembrane temperature difference at element n (K)
T_{L_n}, T_{V_n}	L/V temperatures of element n (K)
U_E, U_I	External/internal GLMC heat transfer coefficients (kJ/(h.m ² .K))
\underline{V}_n	Vector of species V molar flowrates leaving element n (mol/s)
v_{L_n}, v_{V_n}	L/V axial velocities at element n (m/s)
X_k, Y_k	L and V species k mol fraction
Z_M, z	GLMC length; GLMC axial position (m)
Greek Symbols	
φ, κ	Packing ratio; Kozeny factor
μ_{L_n}, μ_{V_n}	L/V dynamic viscosities at element n (Pa.s)
Π_k	Transmembrane k mass transfer coefficient (mol/(s.bar.m ²))
$\bar{\rho}_{L_n}, \bar{\rho}_{V_n}$	L/V molar densities at element n (kmol/m ³)

Appendix A. GLMC-PC-D Model Validation

The GLMC-PC-D model was simulated to reproduce the results of de Medeiros et al. [54], where a desulfurized high-pressure NG was decarbonated using a chemical-absorption parallel-contact GLMC with aqueous-MEA-MDEA. The HYSYS Acid-Gas Chemical-Solvents Thermodynamic Package [90] was used, which is based on e-NRTL for chemical-solvent modeling and PR-EOS for the vapor phase [91]. Besides CO₂/CH₄/H₂O, new species of C₂H₆/C₃H₈/C₄H₁₀/C₅H₁₂/MEA/MDEA were included as transferable species of GLMC-PC-D. The same parameters of de Medeiros et al. [54] were adopted (Table A1). $\Pi_{H_2O} = \Pi_{CO_2}$ was assumed because HFM Teflon AF1600 has H₂O/CO₂ selectivity close to 1 [92]. Table A2 shows inlet/outlet streams, while Figure A1 depicts the GLMC-PC-D model's validation by comparing GLMC profiles. Both show GLMC-PC-D model predictions agreeing with de Medeiros et al. [54].

Table A1. Parameters: GLMC model and transmembrane transfer coefficients [54].

Item	Value	Item	Value	Item	Value	Item	Value
D	0.8 m	d_o	0.502 mm	Π_{CO_2}	1.7×10^{-4} mol/(s.bar.m ²)	$\Pi_{C_3H_{12}}$	10^{-10} mol/(s.bar.m ²)
Z_M	2 m	N_{HF}	2.188×10^6	Π_{CH_4}	5.8×10^{-6} mol/(s.bar.m ²)	Π_{MEA}	2×10^{-15} mol/(s.bar.m ²)
Volume	1.005 m ³	A_{GLMC}	6901.4 m ²	$\Pi_{C_2H_6}$	10^{-8} mol/(s.bar.m ²)	Π_{MDEA}	2×10^{-15} mol/(s.bar.m ²)
N_M	40	T^{amb}	27 °C	$\Pi_{C_3H_8}$	10^{-9} mol/(s.bar.m ²)	Π_{H_2O}	1.7×10^{-4} mol/(s.bar.m ²)
d_i	0.5 mm	U_E	5 W/(m ² .K)	$\Pi_{C_4H_{10}}$	5×10^{-10} mol/(s.bar.m ²)	U_I	2 W/(m ² .K)

Table A2. GLMC-PC-D model validation by de Medeiros et al. [54]: inlet/outlet streams.

	Solvent Inlet	CO ₂ -Rich NG Inlet	Treated Gas [54]	Treated-Gas GLMC-PC-D
P (bar)	5.0	50.0	49.85	49.85
T (°C)	26.85	26.85	38.80	39.77
MMNm³/d	-	1.0	0.830	0.829
kg/h	17,651	-	-	-
CO₂ (%mol)	0	10.19	3.50	3.36
CH₄ (%mol)	0	73.22	76.5	76.41
C₂H₆ (%mol)	0	9.09	11.00	10.97
C₃H₈ (%mol)	0	4.25	5.10	5.14
C₄H₁₀ (%mol)	0	1.78	2.20	2.15
C₅H₁₂ (%mol)	0	1.47	1.80	1.77
H₂O (%mol)	60	0	0	0.20
MEA (%mol)	20	0	0	3.26×10^{-17}
MDEA (%mol)	20	0	0	1.23×10^{-17}

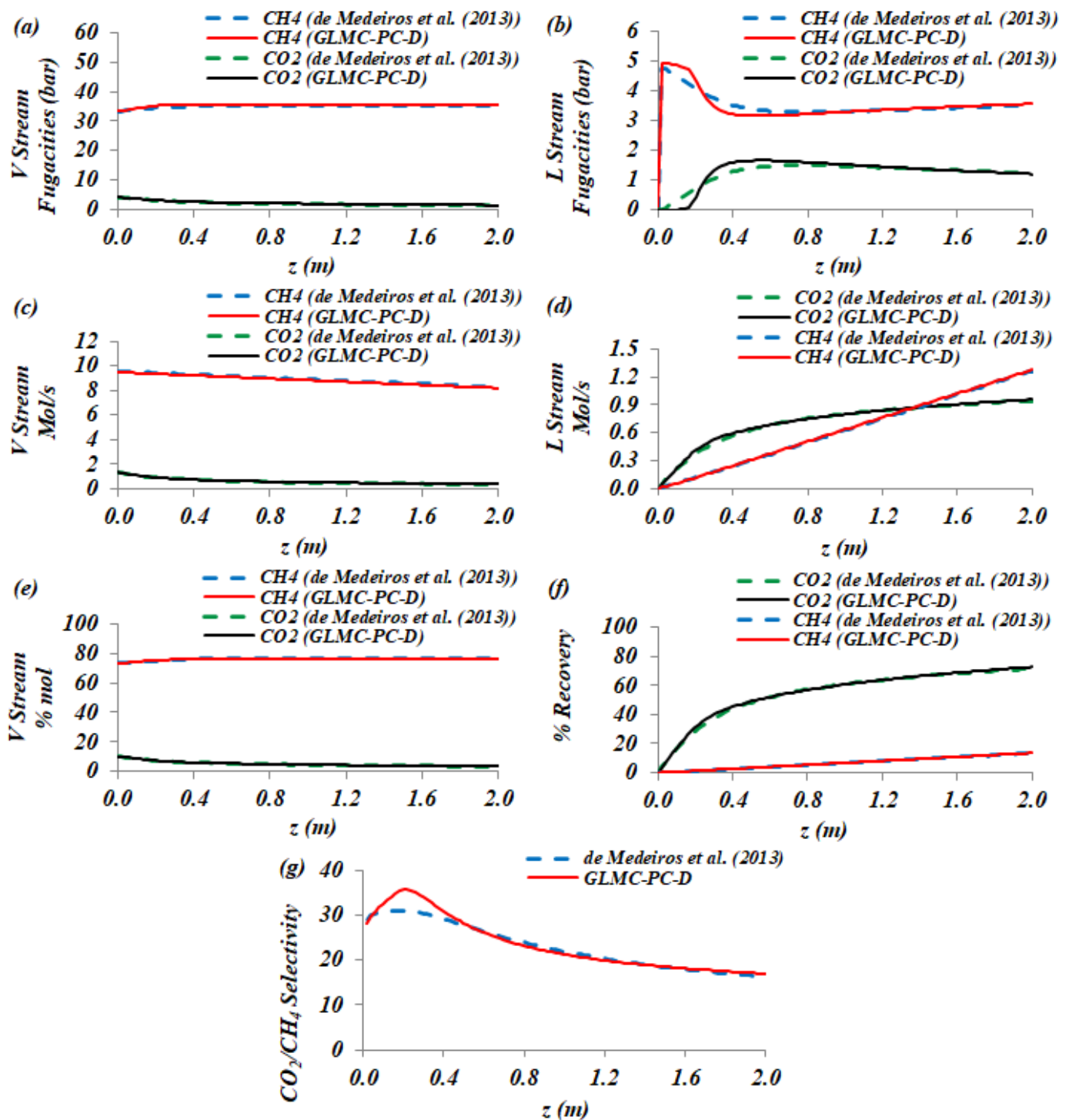


Figure A1. GLMC-PC-D model validation by de Medeiros et al. [54]: profiles versus z (m): (a) V fugacities (bar); (b) L fugacities (bar); (c) V flowrates (mol/s); (d) L flowrates (mol/s); (e) V composition (%mol); (f) %recovery; (g) CO_2/CH_4 selectivity.

Appendix B. GLMC-PC-D Model Asymptotic Validation with P-H Flash

Large parallel-contact (co-current) adiabatic GLMC batteries should approach the response of an adiabatic gas–liquid direct-contact P-H flash because, with a large parallel-contact area, GLMC outlet streams nearly achieve adiabatic energy-constrained VLE at a given pressure. Thus, an adiabatic GLMC-PC-D model was simulated with a large battery area (54 modules) for an asymptotic comparison with HYSYS 10.0 P-H flash. The same

desulfurized high-pressure NG in Appendix A is decarbonated by a chemical-absorption parallel-contact GLMC with aqueous-MEA-MDEA. Table A1 parameters (except $U_E = 0$ for the adiabatic GLMC) and Table A2 inlet streams were adopted with $P = 50$ bar for both feeds. The HYSYS 10.0 Acid-Gas Chemical-Solvents Package was used in the GLMC-PC-D model and P-H flash. Figure A2 shows GLMC-PC-D fugacity profiles, where the vanishing $\text{CO}_2/\text{CH}_4/\text{H}_2\text{O}$ V/L fugacity differences evince that the GLMC battery is sufficiently large enough to achieve VLE for the main transferable species.

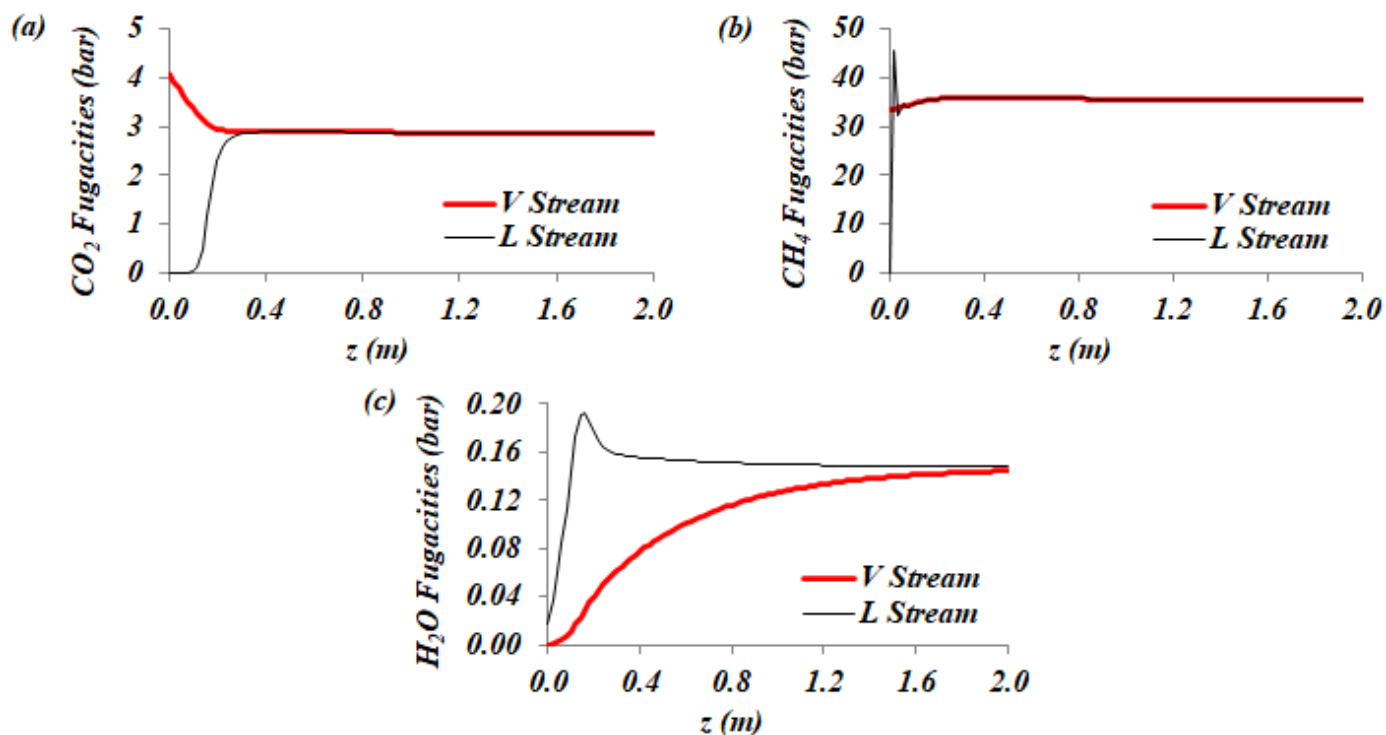


Figure A2. GLMC-PC-D V/L fugacity profiles: (a) CO_2 ; (b) CH_4 ; (c) H_2O .

Table A3 depicts a comparison of the outlet streams, where V/L outlet temperatures and pressures perfectly match, as well as the treated-gas CO_2 , water, and hydrocarbon outlet compositions. V and L flowrates in kmol/h are in excellent agreement, since the numerical differences are about 0.2%. CO_2 -rich solvent outlet compositions are also in excellent agreement. The slight differences are because the GLMC-PC-D model approached the asymptotic limit of adiabatic P-H flash, but was not exactly equal to it. For the asymptotic limit, we expected a slightly higher transference of water $\text{L} \rightarrow \text{V}$ and hydrocarbon $\text{V} \rightarrow \text{L}$, enhancing the solvent hydrocarbons and lowering solvent CO_2 and H_2O outlet compositions in %mol.

In Figure A3, HYSYS 10.0 P-H flash outlet streams are outlined with dashed lines along the GLMC axial direction, while L/V GLMC-PC-D profiles appear as solid lines. The results of the large GLMC-PC-D model asymptotically agree with P-H flash, as seen in Table A3 and in Figure A3a–g. Particularly, in Figure A3g, the order of magnitude of the CH_4 L flowrate is 10^{-3} mol/s. In this case, in absolute terms, the error magnitude reaches 0.005 mol/s, a small value. But, in relative terms, the error magnitude reaches 150%. Considering the absolute error magnitude, these numbers are considered to be in good agreement. The temperature profiles of the GLMC-PC-D model also asymptotically converge to the flash temperature (65.9°C) in Figure A3h.

Table A3. GLMC-PC-D model's asymptotic validation with HYSYS 10.0 P-H flash: outlet streams.

	CO ₂ -Rich Solvent P-H Flash	CO ₂ -Rich Solvent GLMC-PC-D	Treated-Gas P-H Flash	Treated-Gas GLMC-PC-D
P (bar)	50.0	50.0	50.0	50.0
T (°C)	65.90	65.90	65.90	65.90
kmol/h	440.4	439.3	1796.4	1797.5
kg/h	20,629	20,605	39,302	39,326
CO ₂ (%mol)	15.94	15.99	6.64	6.64
CH ₄ (%mol)	0.31	0.12	75.74	75.74
C ₂ H ₆ (%mol)	0.06	0.01	9.40	9.40
C ₃ H ₈ (%mol)	0.02	4.40×10^{-4}	4.40	4.40
C ₄ H ₁₀ (%mol)	0.01	6.55×10^{-5}	1.52	1.52
C ₅ H ₁₂ (%mol)	0.01	1.65×10^{-5}	1.84	1.84
H ₂ O (%mol)	49.43	49.58	0.46	0.46
MEA (%mol)	17.11	17.15	1.09×10^{-4}	5.87×10^{-15}
MDEA (%mol)	17.11	17.15	2.39×10^{-4}	4.53×10^{-15}

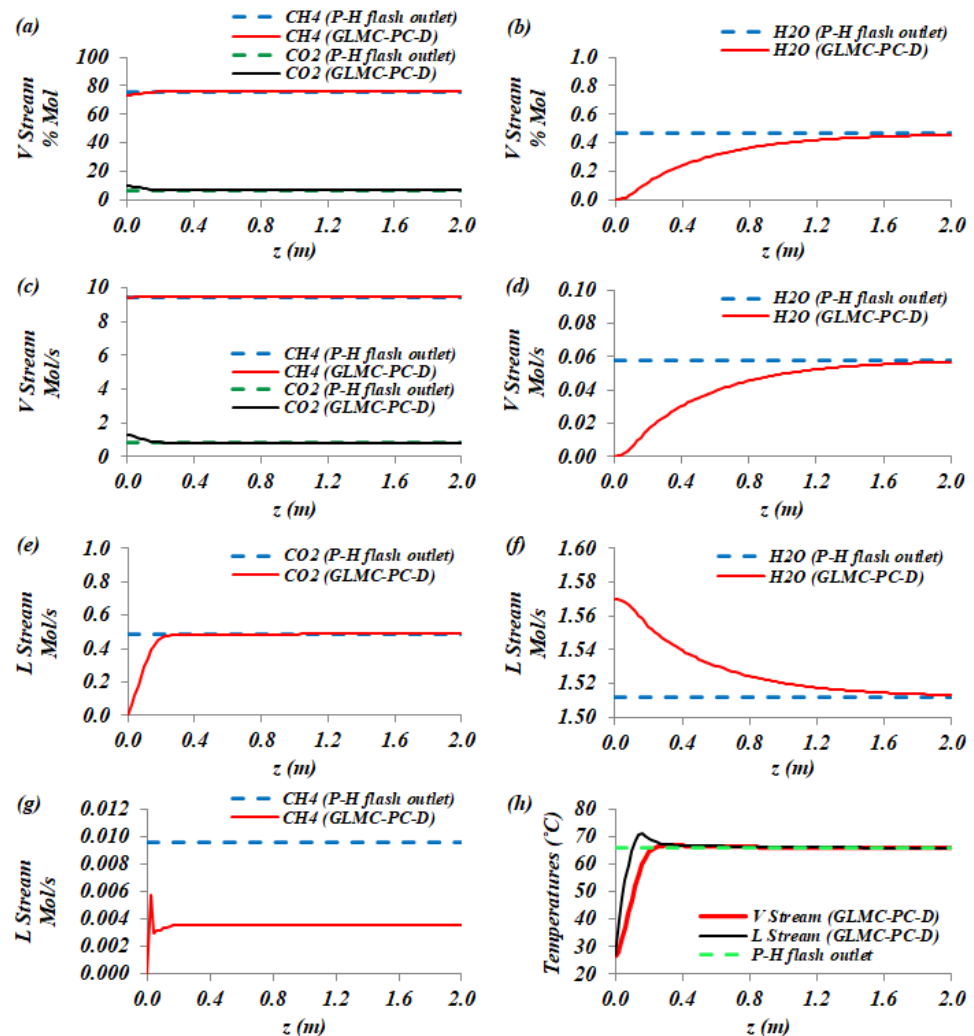


Figure A3. GLMC-PC-D asymptotic validation with HYSYS P-H flash—profiles versus z (m). V (%mol); (a) CO₂/CH₄ (b) H₂O; (c) CO₂/CH₄ V (mol/s) (d) H₂O; V (mol/s); (e) CO₂ L (mol/s); (f) H₂O L (mol/s); (g) CH₄ L (mol/s) (h) Temperatures (°C): V and L.

Appendix C. GLMC-CCC-D Asymptotic Validation with an Adiabatic Absorption Column

Another asymptotic GLMC-UOE validation is conducted to assess countercurrent contact. This time, a large-area adiabatic countercurrent GLMC battery must achieve the results of a large adiabatic absorption column. Thus, the results of a large GLMC-CCC-D battery (9 modules, $M = 5$ elements) are compared with the counterparts of a large HYSYS 10.0 countercurrent absorber ($Stages = 18$) with bottom NG feed and top solvent feed. The desulfurized high-pressure NG in Appendix A is decarbonated by a countercurrent chemical-absorption GLMC with aqueous-MEA-MDEA. The HYSYS Acid-Gas Chemical-Solvents Package was adopted used the GLMC-CCC-D model and absorption column. Since the solvent-CO₂ weight ratio (capture-ratio) is small in this case, nine GLMC-CCC-D modules would require quite a large battery and an 18-staged column is also large (i.e., absorption is limited to the five upper column stages). The data from Table A1 (except U_I and U_E) and inlet streams from Table A2 (both feeds at 50 bar) were used. For the adiabatic GLMC-CCC-D model, $U_E = 0$ was chosen and the internal GLMC-CCC-D heat transfer adopted the product $U_I A_I$ of the GLMC-PC-D model (Appendix B), i.e., $U_I^{GLMC-CCC-L} = 12W/(m^2.K)$. The GLMC-CCC-D model predictions adhere to the absorber column results (Table A4).

Table A4. GLMC-CCC-D model asymptotic validation with HYSYS absorber: outlet streams.

Item	CO ₂ -Rich Solvent Absorber	CO ₂ -Rich Solvent GLMC-CCC-D	Treated-Gas Absorber	Treated-Gas GLMC-CCC-D
P (bar)	50.0	50.0	50.0	50.0
T (°C)	26.53	40.12	91.75	89.87
kmol/h	444.0	456.9	1792.8	1779.9
kg/h	21,182	21,185	38,749	38,746
CO ₂ (%mol)	20.09	17.59	5.60	6.13
CH ₄ (%mol)	0.11	0.11	75.93	76.48
C ₂ H ₆ (%mol)	0.04	1.67×10^{-3}	9.42	9.50
C ₃ H ₈ (%mol)	0.02	6.71×10^{-5}	4.41	4.44
C ₄ H ₁₀ (%mol)	0.01	9.77×10^{-6}	1.52	1.54
C ₅ H ₁₂ (%mol)	0.01	2.46×10^{-6}	1.86	1.86
H ₂ O (%mol)	45.81	49.32	1.26	0.05
MEA (%mol)	16.95	16.49	4.17×10^{-3}	4.85×10^{-16}
MDEA (%mol)	16.96	16.49	2.35×10^{-3}	4.85×10^{-16}

Appendix D. GLMC-CCC-D Model Validation: Water Solvent GLMC

GLMC-CCC-D mass transfer and pressure-drop validations were performed by reproducing the results of Belaisaoui and Favre [47], where CO₂ is removed from a desulfurized biogas by a GLMC-Absorber with pressurized water, while a GLMC-Stripper regenerates the solvent with nitrogen ($P = 1$ atm). In this process [47], CO₂/CH₄ is transferred with $Selectivity^{CO_2/CH_4} = 17$, but H₂O/N₂ is supposedly non-transferable and the GLMC is adiabatic producing isothermal results. Figure A4 depicts the system of Belaisaoui and Favre [47].

For the GLMC-CCC-D simulation ($M = 5$ elements), the HYSYS Acid-Gas Physical-Solvents Thermodynamic Package [81] was selected. GLMC modules and the capture ratio of Belaisaoui and Favre [47] were used (Table 2). Transmembrane transfer coefficients of components (Π_k) were not informed. Thus, Π_{CO_2} and Π_{CH_4} were estimated to adhere to the GLMC-CCC-D predictions of Belaisaoui and Favre [47]. $\Pi_{H_2O} = \Pi_{N_2} = 0$ was set to turn off H₂O/N₂ transfers. With $2 W/m^2.K$ [54], the GLMC-CCC-D calibration was performed to reproduce the CO₂/CH₄ transfers by Belaisaoui and Favre [47] leading to $\Pi_{CO_2} = 6.5756 \times 10^{-4} \text{ mol}/(s.bar.m^2)$ and $\Pi_{CH_4} = 3.8680 \times 10^{-5} \text{ mol}/(s.bar.m^2)$, which were applied to simulate both the GLMC-Absorber and GLMC-Stripper. Table A5, presenting the outlet streams and process results, summarizes the GLMC-CCC-D model's

validation against Belaisaoui and Favre [47]. It is seen that the GLMC-CCC-D model agrees with Belaisaoui's and Favre's [47] results. Thus, Π_{CO_2} and Π_{CH_4} were adopted in this work (Table 2) for landfill-gas decarbonation with water.

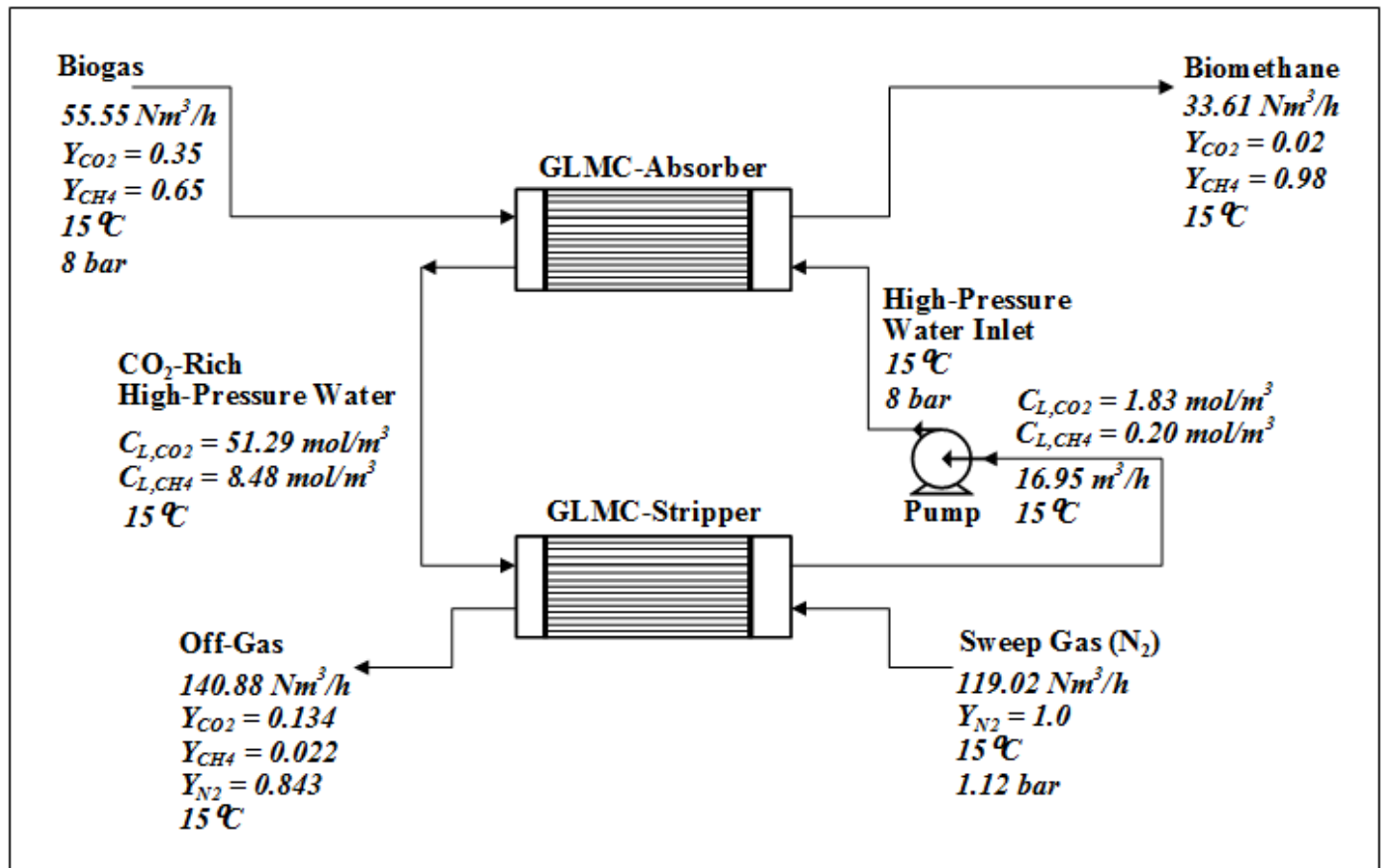


Figure A4. GLMC biogas purification [47].

Table A5. GLMC-CCC-D model validation by Belaisaoui and Favre [47]: outlet streams.

	Biomethane [47]	Biomethane GLMC-CCC-D	Off Gas [47]	Off-Gas GLMC-CCC-D
P (bar)	--	7.996	--	0.6831
T (°C)	15	15.25	15	18.37
Nm ³ /h	33.61	33.73	140.88	141.55
CO ₂ (%mol)	2	2	13.4	13.7
CH ₄ (%mol)	98	98	2.2	2.2
N ₂ (%mol)	0	0	84.3	84.1
Process: General Results				
	Belaisaoui and Favre [47]		GLMC-CCC-D	
Liquid Pressure Drop (bar)	2.43		2.47	
CO ₂ %Removal	96.65		96.53	
CH ₄ %Loss	8.7		8.5	
CO ₂ -Rich Solvent Temperature (°C)	15		15.26	
Regenerated Solvent Temperature (°C)	15		15.03	

Appendix E. GLMC Internal Heat Transfer Coefficient for Landfill-Gas Purification

For the simulation of GLMC landfill-gas purification using physical-solvent water, the internal heat transfer coefficient, U_I , has to be chosen, because the only available $U_I = 2 \text{ W/m}^2\cdot\text{K}$ comes from a chemical-absorption GLMC [54]. Thus, U_I was estimated by asymptotically comparing the thermal performances of a large adiabatic GLMC-CCC-D battery for landfill-gas purification (Table 2) using water ($T = 15 \text{ }^\circ\text{C}$, $P = 7 \text{ bar}$) against a large adiabatic 30-staged absorption column with water fed through the top ($T = 15 \text{ }^\circ\text{C}$, $P = 7 \text{ bar}$) and landfill-gas through the bottom ($P = 7.1 \text{ bar}$). Theoretically, these two large adiabatic countercurrent operations should provide similar composition and thermal results. We emphasize that this stratagem is only being used to estimate a feasible U_I , i.e., this is not a calibration. Indeed, there are innumerable U_I values that match the large column thermal response. Table 2 shows the inlet streams. The GLMC-CCC-D battery has $N_M = 780$ modules. Π_{CO_2} and Π_{CH_4} come from Appendix D, with $\Pi_{\text{H}_2\text{O}} = \Pi_{\text{CO}_2}$ [92], $\Pi_{\text{H}_2\text{S}} = \Pi_{\text{CO}_2}$, and $U_E = 0$. U_I was manipulated until the GLMC-CCC-D model's outlet temperatures approached the column counterparts in Table A6. The estimated $U_I = 0.09 \text{ W/m}^2\cdot\text{K}$ was adopted for the GLMC-CCC-D and GLMC-PC-D simulations using water for landfill-gas purification (Table 2).

Table A6. GLMC-CCC-D U_I estimation with the HYSYS 10.0 absorber.

Item	CO ₂ -Rich Water Absorber	CO ₂ -Rich Water GLMC-CCC-D	Treated-Gas Absorber	Treated-Gas GLMC-CCC-D
P (bar)	7.1	6.664	7.0	6.998
T (°C)	15.37	15.37	15.02	15.08
MMNm ³ /d	-	-	0.252957	0.253672
kg/h	7,276,541	7,276,586	-	-
CH ₄ (%mol)	0.01	0.01	99.10	99.10
CO ₂ (%mol)	0.09	0.09	0.64	0.13
H ₂ S (ppm-mol)	0.346	0.346	5×10^{-5}	5×10^{-5}
H ₂ O (%mol)	99.90	99.90	0.26	0.26

References

1. Popov, V. A new landfill system for cheaper landfill gas purification. *Renew. Energy* **2005**, *30*, 1021–1029. [[CrossRef](#)]
2. Yang, L.; Ge, X.; Wan, C.; Yu, F.; Li, Y. Progress and perspectives in converting biogas to transportation fuels. *Renew. Sustain. Energy Rev.* **2014**, *40*, 1133–1152. [[CrossRef](#)]
3. Zhou, K.; Chaemchuen, S.; Verpoort, F. Alternative materials in technologies for biogas upgrading via CO₂ capture. *Renew. Sustain. Energy Rev.* **2017**, *79*, 1414–1441. [[CrossRef](#)]
4. Wise, D.L.; Kispert, R.G.; Langton, E.W. A review of bioconversion systems for energy recovery from municipal solid waste part II: Fuel gas production. *Resour. Conserv.* **1981**, *6*, 117–136. [[CrossRef](#)]
5. Parker, N.; Williams, R.; Dominguez-Faus, R.; Scheitrum, D. Renewable natural gas in California: An assessment of the technical and economic potential. *Energy Policy* **2017**, *111*, 235–245. [[CrossRef](#)]
6. Nadaletti, W.C.; Cremonez, P.A.; de Souza, S.N.M.; Bariccatti, R.A.; Belli Filho, P.; Secco, D. Potential use of landfill biogas in urban bus fleet in the Brazilian states: A review. *Renew. Sustain. Energy Rev.* **2015**, *41*, 277–283. [[CrossRef](#)]
7. Keogh, N.; Corr, D.; Monaghan, R.F.D. Biogenic renewable gas injection into natural gas grids: A review of technical and economic modelling studies. *Renew. Sustain. Energy Rev.* **2022**, *168*, 112818. [[CrossRef](#)]
8. Schipfer, F.; Mäki, E.; Schmieder, U.; Lange, N.; Schildhauer, T.; Hennig, C.; Thrän, D. Status of and expectations for flexible bioenergy to support resource efficiency and to accelerate the energy transition. *Renew. Sustain. Energy Rev.* **2022**, *158*, 112094. [[CrossRef](#)]
9. Araújo, O.Q.F.; de Medeiros, J.L. How is the transition away from fossil fuels doing, and how will the low-carbon future unfold? *Clean Technol. Environ. Policy* **2021**, *23*, 1385–1388. [[CrossRef](#)]
10. Araújo, O.Q.F.; Boa Morte, I.B.; Borges, C.L.T.; Morgado, C.R.V.; de Medeiros, J.L. Beyond clean and affordable transition pathways: A review of issues and strategies to sustainable energy supply. *Int. J. Electr. Power Energy Syst.* **2024**, *155*, 109544. [[CrossRef](#)]
11. Yu, H.; Xu, H.; Fan, J.; Zhu, Y.B.; Wang, F.; Wu, H. Transport of shale gas in microporous/nanoporous media: Molecular to pore-scale simulations. *Energy Fuels* **2021**, *35*, 911–943. [[CrossRef](#)]
12. Brigagão, G.V.; de Medeiros, J.L.; Araújo, O.Q.F.; Mikulčić, H.; Duić, N. A zero-emission sustainable landfill-gas-to-wire oxyfuel process: Bioenergy with carbon capture and sequestration. *Renew. Sustain. Energy Rev.* **2021**, *138*, 110686. [[CrossRef](#)]

13. Ruoso, A.C.; Nora, M.D.; Siluk, J.C.M.; Ribeiro, J.L.D. The impact of landfill operation factors on improving biogas generation in Brazil. *Renew. Sustain. Energy Rev.* **2022**, *154*, 111868. [[CrossRef](#)]
14. Khan, M.U.; Lee, J.T.E.; Bashir, M.A.; Dissanayake, P.D.; Ok, Y.S.; Tong, Y.W.; Shariati, M.A.; Wu, S.; Ahring, B.K. Current status of biogas upgrading for direct biomethane use: A review. *Renew. Sustain. Energy Rev.* **2021**, *149*, 111343. [[CrossRef](#)]
15. Araújo, O.Q.F.; Reis, A.C.; de Medeiros, J.L.; do Nascimento, J.F.; Grava, W.M.; Musse, A.P.S. Comparative analysis of separation technologies for processing carbon dioxide rich natural gas in ultra-deepwater oil fields. *J. Clean. Prod.* **2017**, *155*, 12–22. [[CrossRef](#)]
16. Keshavarz, P.; Fathikalajahi, J.; Ayatollahi, S. Mathematical modeling of the simultaneous absorption of carbon dioxide and hydrogen sulfide in a hollow fiber membrane contactor. *Sep. Purif. Technol.* **2008**, *63*, 145–155. [[CrossRef](#)]
17. Mokhatab, S.; Poe, W.A. *Handbook of Natural Gas Transmission and Processing—Principles and Practices*, 2nd ed.; Gulf Professional Publishing: Houston, TX, USA, 2012.
18. Oshita, K.; Omori, K.; Takaoka, M.; Mizuno, T. Removal of siloxanes in sewage sludge by thermal treatment with gas stripping. *Energy Convers. Manag.* **2014**, *81*, 290–297. [[CrossRef](#)]
19. de Arespachoga, N.; Valderrama, C.; Raich-Montiu, J.; Crest, M.; Mehta, S.; Cortina, J.L. Understanding the effects of the origin, occurrence, monitoring, control, fate and removal of siloxanes on the energetic valorization of sewage biogas—A review. *Renew. Sustain. Energy Rev.* **2015**, *52*, 366–381. [[CrossRef](#)]
20. Surita, S.C.; Tansel, B. Preliminary investigation to characterize deposits forming during combustion of biogas from anaerobic digesters and landfills. *Renew. Energy* **2015**, *80*, 674–681. [[CrossRef](#)]
21. Scholz, M.; Melin, T.; Wessling, M. Transforming biogas into biomethane using membrane technology. *Renew. Sustain. Energy Rev.* **2013**, *17*, 199–212. [[CrossRef](#)]
22. Leung, D.Y.C.; Caramanna, G.; Maroto-Valer, M.M. An overview of current status of carbon dioxide capture and storage technologies. *Renew. Sustain. Energy Rev.* **2014**, *39*, 426–443. [[CrossRef](#)]
23. Pour, N.; Webley, P.A.; Cook, P.J. Potential for using municipal solid waste as a resource for bioenergy with carbon capture and storage (BECCS). *Int. J. Greenh. Gas. Control* **2018**, *68*, 1–15. [[CrossRef](#)]
24. Milão, R.F.D.; Carminati, H.B.; Araújo, O.Q.F.; de Medeiros, J.L. Thermodynamic, financial and resource assessments of a large-scale sugarcane-biorefinery: Prelude of full bioenergy carbon capture and storage scenario. *Renew. Sustain. Energy Rev.* **2019**, *113*, 109251. [[CrossRef](#)]
25. Kemper, J. Biomass and carbon dioxide capture and storage: A review. *Int. J. Greenh. Gas. Control* **2015**, *40*, 401–430. [[CrossRef](#)]
26. Gong, H.; Zhou, S.; Chen, Z.; Chen, L. Effect of volatile organic compounds on carbon dioxide adsorption performance via pressure swing adsorption for landfill gas upgrading. *Renew. Energy* **2019**, *135*, 811–818. [[CrossRef](#)]
27. Gaur, A.; Park, J.W.; Maken, S.; Song, H.J.; Park, J.J. Landfill gas (LFG) processing via adsorption and alkanolamine absorption. *Fuel Process. Technol.* **2010**, *91*, 635–640. [[CrossRef](#)]
28. Tay, W.H.; Lau, K.K.; Lai, L.S.; Shariff, A.M.; Wang, T. Current development and challenges in the intensified absorption technology for natural gas purification at offshore condition. *J. Nat. Gas. Sci. Eng.* **2019**, *71*, 102977. [[CrossRef](#)]
29. Tao, J.; Wang, J.; Zhu, L.; Chen, X. Integrated design of multi-stage membrane separation for landfill gas with uncertain feed. *J. Membr. Sci.* **2019**, *590*, 117260. [[CrossRef](#)]
30. Baker, R.W.; Lokhandwala, K. Natural Gas Processing with Membranes: An Overview. *Ind. Eng. Chem. Res.* **2008**, *47*, 2109–2121. [[CrossRef](#)]
31. Moreira, L.C.; Borges, P.O.; Cavalcante, R.M.; Young, A.F. Simulation and economic evaluation of process alternatives for biogas production and purification from sugarcane vinasse. *Renew. Sustain. Energy Rev.* **2022**, *163*, 112532. [[CrossRef](#)]
32. Siagian, U.W.R.; Raksajati, A.; Himma, N.F.; Khoiruddin, K.; Wenten, I.G. Membrane-based carbon capture technologies: Membrane gas separation vs. membrane contactor. *J. Nat. Gas. Sci. Eng.* **2019**, *67*, 172–195. [[CrossRef](#)]
33. Buonomenna, M.G.; Bae, J. Membrane processes and renewable energies. *Renew. Sustain. Energy Rev.* **2015**, *43*, 1343–1398. [[CrossRef](#)]
34. Ramezani, R.; Di Felice, L.; Gallucci, F. A Review on Hollow Fiber Membrane Contactors for Carbon Capture: Recent Advances and Future Challenges. *Processes* **2022**, *10*, 2103. [[CrossRef](#)]
35. Sirkar, K.K.; Fane, A.G.; Wang, R.; Wickramasinghe, S.R. Process intensification with selected membrane processes. *Chem. Eng. Process. Process Intensif.* **2015**, *87*, 16–25. [[CrossRef](#)]
36. Asfand, F.; Bourouis, M. A review of membrane contactors applied in absorption refrigeration systems. *Renew. Sustain. Energy Rev.* **2015**, *45*, 173–191. [[CrossRef](#)]
37. Lee, Y.; Park, Y.J.; Lee, J.; Bae, T.H. Recent advances and emerging applications of membrane contactors. *Chem. Eng. J.* **2023**, *461*, 141948. [[CrossRef](#)]
38. Amaral, R.A.; Habert, C.A.; Borges, C.P. Performance evaluation of composite and microporous gas-liquid membrane contactors for CO₂ removal from a gas mixture. *Chem. Eng. Process. Process Intensif.* **2016**, *102*, 202–209. [[CrossRef](#)]
39. Zhang, H.Y.; Wang, R.; Liang, D.T.; Tay, J.H. Modeling and experimental study of CO₂ absorption in a hollow fiber membrane contactor. *J. Membr. Sci.* **2006**, *279*, 301–310. [[CrossRef](#)]
40. Yin, Y.; Cao, Z.; Gao, H.; Sema, T.; Na, Y.; Xiao, M.; Liang, Z.; Tontiwachwuthikul, P. Experimental Measurement and Modeling Prediction of Mass Transfer in a Hollow Fiber Membrane Contactor Using Tertiary Amine Solutions for CO₂ Absorption. *Ind. Eng. Chem. Res.* **2022**, *61*, 9632–9643. [[CrossRef](#)]

41. Lee, H.J.; Kim, M.K.; Park, J.H.; Magnone, E. Temperature and pressure dependence of the CO₂ absorption through a ceramic hollow fiber membrane contactor module. *Chem. Eng. Process. Process Intensif.* **2020**, *150*, 107871. [[CrossRef](#)]
42. Saidi, M.; Inaloo, E.B. CO₂ removal using 1DMA2P solvent via membrane technology: Rate based modeling and sensitivity analysis. *Chem. Eng. Process. Process Intensif.* **2021**, *166*, 108464. [[CrossRef](#)]
43. Koonaphaddeert, S.; Wu, Z.; Li, K. Carbon dioxide stripping in ceramic hollow fibre membrane contactors. *Chem. Eng. Sci.* **2009**, *64*, 1–8. [[CrossRef](#)]
44. da Cunha, G.P.; de Medeiros, J.L.; Araújo, O.Q.F. Carbon Capture from CO₂-Rich Natural Gas via Gas-Liquid Membrane Contactors with Aqueous-Amine Solvents: A Review. *Gases* **2022**, *2*, 98–133. [[CrossRef](#)]
45. Teplyakov, V.V.; Okunev, A.Y.; Laguntsov, N.I. Computer design of recycle membrane contactor systems for gas separation. *Sep. Purif. Technol.* **2007**, *57*, 450–454. [[CrossRef](#)]
46. Belaissaoui, B.; Claveria-Baro, J.; Lorenzo-Hernando, A.; Zaidiza, D.A.; Chabanon, E.; Castel, C.; Rode, S.; Roizard, D.; Favre, E. Potentialities of a dense skin hollow fiber membrane contactor for biogas purification by pressurized water absorption. *J. Membr. Sci.* **2016**, *513*, 236–249. [[CrossRef](#)]
47. Belaissaoui, B.; Favre, E. Novel dense skin hollow fiber membrane contactor based process for CO₂ removal from raw biogas using water as absorbent. *Sep. Purif. Technol.* **2018**, *193*, 112–126. [[CrossRef](#)]
48. Fougérit, V.; Pozzobon, V.; Pareau, D.; Théoleyre, M.A.; Stambouli, M. Experimental and numerical investigation binary mixture mass transfer in a gas-liquid membrane contactor. *J. Membr. Sci.* **2019**, *572*, 1–11. [[CrossRef](#)]
49. Li, Y.; Wang, L.; Jin, P.; Song, X.; Zhan, X. Removal of carbon dioxide from pressurized landfill gas by physical absorbents using a hollow fiber membrane contactor. *Chem. Eng. Process. Process Intensif.* **2017**, *121*, 149–161. [[CrossRef](#)]
50. Li, Y.; Wang, L.; Hu, X.; Jin, P.; Song, X. Surface modification to produce superhydrophobic hollow fiber membrane contactor to avoid membrane wetting for biogas purification under pressurized conditions. *Sep. Purif. Technol.* **2018**, *194*, 222–230. [[CrossRef](#)]
51. Tantikhajongosol, P.; Laosiripojana, N.; Jiraratananon, R.; Assabumrungrat, S. A modeling study of module arrangement and experimental investigation of single stage module for physical absorption of biogas using hollow fiber membrane contactors. *J. Membr. Sci.* **2018**, *549*, 283–294. [[CrossRef](#)]
52. Nakhjiri, A.T.; Heydarinasab, A. Computational simulation and theoretical modeling of CO₂ separation using EDA, PZEA and PS absorbents inside the hollow fiber membrane contactor. *J. Ind. Eng. Chem.* **2019**, *78*, 106–115. [[CrossRef](#)]
53. Ghasem, N.; Al-Marzouqi, M.; Rahim, N.A. Modeling of CO₂ absorption in a membrane contactor considering solvent evaporation. *Sep. Purif. Technol.* **2013**, *110*, 1–10. [[CrossRef](#)]
54. de Medeiros, J.L.; Nakao, A.; Grava, W.M.; Nascimento, J.F.; Araújo, O.Q.F. Simulation of an offshore natural gas purification process for CO₂ removal with gas-liquid contactors employing aqueous solutions of ethanolamines. *Ind. Eng. Chem. Res.* **2013**, *52*, 7074–7089. [[CrossRef](#)]
55. de Medeiros, J.L.; Barbosa, L.C.; Araújo, O.Q.F. Equilibrium approach for CO₂ and H₂S absorption with aqueous solutions of alkanolamines: Theory and parameter estimation. *Ind. Eng. Chem. Res.* **2013**, *52*, 9203–9226. [[CrossRef](#)]
56. Huang, M.; Xu, H.; Yu, H.; Zhang, H.; Micheal, M.; Yuan, X.; Wu, H. Fast prediction of methane adsorption in shale nanopores using kinetic theory and machine learning algorithm. *Chem. Eng. J.* **2022**, *446*, 137221. [[CrossRef](#)]
57. Aguado, D.; Noriega-Hevia, G.; Serralta, J.; Seco, A. Using machine learning techniques to predict ammonium concentration in membrane contactors for nitrogen recovery as a valuable resource. *Eng. Appl. Artif. Intell.* **2023**, *126*, 107330. [[CrossRef](#)]
58. Yarveicy, H.; Ghiasi, M.M.; Mohammadi, A.H. Performance evaluation of the machine learning approaches in modeling of CO₂ equilibrium absorption in piperazine aqueous solution. *J. Mol. Liq.* **2018**, *255*, 375–383. [[CrossRef](#)]
59. Yu, H.; Zhu, Y.; Jin, X.; Liu, H.; Wu, H. Multiscale simulations of shale gas transport in micro/nano-porous shale matrix considering pore structure influence. *J. Nat. Gas. Sci. Eng.* **2019**, *64*, 28–40. [[CrossRef](#)]
60. Ng, E.L.H.; Lau, K.K.; Lau, W.J.; Ahmad, F. Holistic review on the recent development in mathematical modelling and process simulation of hollow fiber membrane contactor for gas separation process. *J. Ind. Eng. Chem.* **2021**, *104*, 231–257. [[CrossRef](#)]
61. Hoff, K.A.; Juliussen, O.; Falk-Pedersen, O.; Svendsen, H.F. Modeling and Experimental Study of Carbon Dioxide Absorption in Aqueous Alkanolamine Solutions Using a Membrane Contactor. *Ind. Eng. Chem. Res.* **2004**, *43*, 4908–4921. [[CrossRef](#)]
62. Hoff, K.A.; Svendsen, H.F. CO₂ absorption with membrane contactors vs. packed absorbers—Challenges and opportunities in post combustion capture and natural gas sweetening. *Energy Procedia* **2013**, *37*, 952–960. [[CrossRef](#)]
63. Quek, V.C.; Shah, N.; Chachuat, B. Modeling for design and operation of high-pressure membrane contactors in natural gas sweetening. *Chem. Eng. Res. Des.* **2018**, *132*, 1005–1019. [[CrossRef](#)]
64. Quek, V.C.; Shah, N.; Chachuat, B. Plant-wide assessment of high-pressure membrane contactors in natural gas sweetening—Part I: Model development. *Sep. Purif. Technol.* **2021**, *258*, 117898. [[CrossRef](#)]
65. Quek, V.C.; Shah, N.; Chachuat, B. Plant-wide assessment of high-pressure membrane contactors in natural gas sweetening—Part II: Process analysis. *Sep. Purif. Technol.* **2021**, *258*, 117938. [[CrossRef](#)]
66. Kerber, J.; Repke, J.U. Mass transfer and selectivity analysis of a dense membrane contactor for upgrading biogas. *J. Membr. Sci.* **2016**, *520*, 450–464. [[CrossRef](#)]
67. Villeneuve, K.; Zaidiza, D.A.; Roizard, D.; Rode, S. Modeling and simulation of CO₂ capture in aqueous ammonia with hollow fiber composite membrane contactors using a selective dense layer. *Chem. Eng. Sci.* **2018**, *190*, 345–360. [[CrossRef](#)]
68. Villeneuve, K.; Hernandez, A.A.T.; Zaidiza, D.A.; Roizard, D.; Rode, S. Effects of water condensation on hollow fiber membrane contactor performance for CO₂ capture by absorption into a chemical solvent. *J. Membr. Sci.* **2018**, *556*, 365–373. [[CrossRef](#)]

69. Usman, M.; Dai, Z.; Hillestad, M.; Deng, L. Mathematical modeling and validation of CO₂ mass transfer in a membrane contactor using ionic liquids for pre-combustion CO₂ capture. *Chem. Eng. Res. Des.* **2017**, *123*, 377–387. [CrossRef]
70. Usman, M.; Hillestad, M.; Deng, L. Assessment of a membrane contactor process for pre-combustion CO₂ capture by modelling and integrated process simulation. *Int. J. Greenh. Gas. Control* **2018**, *71*, 95–103. [CrossRef]
71. McQuillan, R.V.; Momeni, A.; Alivand, M.S.; Stevens, G.W.; Mumford, K.A. Evaluation of potassium glycinate as a green solvent for direct air capture and modelling its performance in hollow fiber membrane contactors. *Chem. Eng. J.* **2024**, *481*, 148764. [CrossRef]
72. Arinelli, L.O.; Trotta, T.A.F.; Teixeira, A.M.; de Medeiros, J.L.; Araújo, O.Q.F. Offshore processing of CO₂ rich natural gas with supersonic separator versus conventional routes. *J. Nat. Gas. Sci. Eng.* **2017**, *46*, 199–221. [CrossRef]
73. da Cunha, G.P.; de Medeiros, J.L.; Araújo, O.Q.F. Technical evaluation of the applicability of gas-liquid membrane contactors for CO₂ removal from CO₂ rich natural gas streams in offshore rigs. *Mater. Sci. Forum* **2019**, *965*, 29–38. [CrossRef]
74. da Cunha, G.P.; de Medeiros, J.L.; Araújo, O.Q.F. Offshore decarbonation of CO₂-rich natural gas intensified via gas-liquid membrane contactors with blended aqueous-amines. *Chem. Eng. Process. Process Intensif.* **2023**, *191*, 109462. [CrossRef]
75. Ajhar, M.; Travasset, M.; Yüce, S.; Melin, T. Siloxane removal from landfill and digester gas—A technology overview. *Bioresour. Technol.* **2010**, *101*, 2913–2923. [CrossRef] [PubMed]
76. Lantelä, J.; Rasi, S.; Lehtinen, J.; Rintala, J. Landfill gas upgrading with pilot-scale water scrubber: Performance assessment with absorption water recycling. *Appl. Energy* **2012**, *92*, 307–314. [CrossRef]
77. Ryckebosch, E.; Drouillon, M.; Vervaeren, H. Techniques for transformation of biogas to biomethane. *Biomass Bioenergy* **2011**, *35*, 1633–1645. [CrossRef]
78. Ashrafi, O.; Bashiri, H.; Esmaili, A.; Sapoundjiev, H.; Navarri, P. Ejector integration for the cost effective design of the SelexolTM process. *Energy* **2018**, *162*, 380–392. [CrossRef]
79. Faiz, R.; Li, K.; Al-Marzouqi, M. H₂S absorption at high pressure using hollow fibre membrane contactors. *Chem. Eng. Process. Process Intensif.* **2014**, *83*, 33–42. [CrossRef]
80. Li, M.; Zhu, Z.; Zhou, M.; Jie, X.; Wang, L.; Kang, G.; Cao, Y. Removal of CO₂ from biogas by membrane contactor using PTFE hollow fibers with smaller diameter. *J. Membr. Sci.* **2021**, *627*, 119232. [CrossRef]
81. Dymont, J.; Watanasiri, S. *Acid Gas Cleaning Using DEPG Physical Solvents: Validation with Experimental and Plant Data. White Paper*; Aspen Technology Inc.: Houston, TX, USA, 2015; Available online: <https://www.aspentech.com/en/resources/white-papers/acid-gas-cleaning-using-depg-physical-solvents---validation-with-experimental-and-plant-data> (accessed on 28 October 2022).
82. Seader, J.D.; Henley, E.J. *Separation Process Principles*, 2nd ed.; John Wiley & Sons, Inc.: New York, NY, USA, 2006.
83. Chabanon, E.; Bounaceur, R.; Castel, C.; Rode, S.; Roizard, D.; Favre, E. Pushing the limits of intensified CO₂ post-combustion capture by gas-liquid absorption through a membrane contactor. *Chem. Eng. Process. Process Intensif.* **2015**, *91*, 7–22. [CrossRef]
84. Tansel, B.; Surita, S.C. Managing siloxanes in biogas-to-energy facilities: Economic comparison of pre- vs post-combustion practices. *Waste Manag.* **2019**, *96*, 121–127. [CrossRef] [PubMed]
85. ANP—Agência Nacional do Petróleo, Gás Natural e Biocombustíveis. ANP N^o16 (17.6.2008)—DOU 18.6.2008. 2008. Available online: <https://atosoficiais.com.br/anp/resolucao-n-16-2008-dispoe-sobre-as-informacoes-constantas-dos-documentos-da-qualidade-e-o-envio-dos-dados-da-qualidade-dos-combustiveis-produzidos-no-territorio-nacional-ou-importados-e-da-outras-providencias> (accessed on 5 February 2024).
86. Ecker, A.M.; Klein, H.; Peschel, A. Systematic and efficient optimization-based design of a process for CO₂ removal from natural gas. *Chem. Eng. J.* **2022**, *445*, 136178. [CrossRef]
87. Smith, J.M.; Van Ness, H.C.; Abbott, M.M. *Introduction to Chemical Engineering Thermodynamics*, 7th ed.; McGraw-Hill Book: New York, NY, USA, 2005.
88. Kern, D.Q. *Process Heat Transfer*; McGraw-Hill Book: New York, NY, USA, 1950.
89. Mehdipourghazi, M.; Barati, S.; Varaminian, F. Mathematical modeling and simulation of carbon dioxide stripping from water using hollow fiber membrane contactors. *Chem. Eng. Process. Process Intensif.* **2015**, *95*, 159–164. [CrossRef]
90. Chang, Y.T.; Dymont, J. *Jump Start Guide: Acid Gas Cleaning in Aspen HYSYS[®]. A Brief Tutorial (and Supplement to and Online Documentation)*; Aspen Technology Inc.: Houston, TX, USA, 2018; Available online: <https://www.aspentech.com/en/resources/jump-start-guide/acid-gas-cleaning-in-aspen-hysys> (accessed on 5 October 2022).
91. Dymont, J.; Watanasiri, S. *Acid Gas Cleaning Using Amine Solvents: Validation with Experimental and Plant Data. White Paper*; Aspen Technology Inc.: Houston, TX, USA, 2018; Available online: <https://www.aspentech.com/en/resources/white-papers/acid-gas-cleaning-using-amine-solvents---validation-with-experimental-and-plant-data> (accessed on 5 February 2024).
92. Scholes, C.A.; Kanehashi, S.; Stevens, G.W.; Kentish, S.E. Water permeability and competitive permeation with CO₂ and CH₄ in perfluorinated polymeric membranes. *Sep. Purif. Technol.* **2015**, *147*, 203–209. [CrossRef]

Disclaimer/Publisher's Note: The statements, opinions and data contained in all publications are solely those of the individual author(s) and contributor(s) and not of MDPI and/or the editor(s). MDPI and/or the editor(s) disclaim responsibility for any injury to people or property resulting from any ideas, methods, instructions or products referred to in the content.